Title (50-word maximum): Repeated administration of 2-hydroxypropyl-β-cyclodextrin (HPβCD) attenuates the chronic inflammatory response to experimental stroke

Abbreviated Title (50-character maximum): HPβCD attenuates chronic inflammation after stroke

Danielle A. Becktel[1], Jacob C. Zbesko[1], Jennifer B. Frye[1], Amanda G. Chung[1], Megan Hayes[1], Kylie Calderon[1], Jeffrey W. Grover[2], Anna Li[1,3], Frankie G. Garcia[1], Marco A. Tavera-Garcia[1], Rick G. Schnellmann[4], Hsin-Jung Joyce Wu[1,3], Thuy-Vi V. Nguyen[1,5], Kristian P. Doyle*[1,5,6,7,8,9]

[1]Department of Immunobiology, University of Arizona, Tucson, Arizona, 85719, USA

[2]Department of Molecular and Cellular Biology, University of Arizona, Tucson, Arizona, 85719, USA

[3]Arizona Arthritis Center, University of Arizona, Tucson, Arizona, 85719

[4]Department of Pharmacology and Toxicology, University of Arizona, Tucson, Arizona, 85719, USA

[5]Department of Neurology, University of Arizona, Tucson, Arizona, 85719, USA

[6]BIO5 Institute, University of Arizona, Tucson, Arizona, 85719, USA

[7]Arizona Center on Aging, University of Arizona, Tucson, Arizona, 85719, USA

[8]Department of Psychology, University of Arizona, Tucson, Arizona, 85719, USA

[9]Department of Neurosurgery, University of Arizona, Tucson, Arizona, 85719, USA

*To whom correspondence should be addressed

Address for Correspondence:

Kristian P. Doyle, Ph.D.

Department of Immunobiology

University of Arizona

1656 E. Mabel Street, P.O. Box 245221

Tucson, Arizona, 85719

Tel: (1) 520-626-7013

Email: doylekr@arizona.edu

# of Figures: 14

# of Tables: 1 (No multimedia or 3D models in this manuscript)

# of Words in Abstract: 249

# of Words in Introduction: 577

# of Words in Discussion: 1513

Conflict of Interest Statement: The authors declare no competing financial interests.

Acknowledgments: This work was funded by NINDS R01NS096091 (KPD), NIA R01AG063808 (TVN), NIA R21AG062781 (TVN), United States Department of Veterans Affairs I01RX003224 (RGS), NIA T32AG058503-01A1 (DAB), NINDS F31NS105455 (JCZ), and the Fondation Leducq Transatlantic Network of Excellence

Stroke-IMPaCT (KPD). We thank Dr. Oswald Quehenberger (UCSD Lipidomics Core), Branden Lau, and Jonathan Galina-Mehlman (University of Arizona Genetics Core) for their technical assistance with lipidomics and transcriptomics analyses. We also thank Dr. Julia Slone-Murphy (NeuroEdit Ltd) for editing a draft of this manuscript.

Abstract (250 words maximum, including citations)

Globally, more than 67 million people are living with the effects of ischemic stroke. Importantly, many stroke survivors develop a chronic inflammatory response that may contribute to cognitive impairment, a common and debilitating sequela of stroke that is insufficiently studied and currently untreatable. 2-hydroxypropyl-β-cyclodextrin (HPβCD) is an FDA-approved cyclic oligosaccharide that can solubilize and entrap lipophilic substances. The goal of the present study was to determine whether the repeated administration of HPβCD curtails the chronic inflammatory response to stroke by reducing lipid accumulation within stroke infarcts in a distal middle cerebral artery occlusion mouse model of stroke. To achieve this goal, we subcutaneously injected young adult and aged male mice with vehicle or HPβCD three times per week, with treatment beginning one week after stroke. We evaluated mice at 7 weeks following stroke using immunostaining, RNA sequencing, lipidomics, and behavioral analyses. Chronic stroke infarct and peri-infarct regions of HPβCD-treated mice were characterized by an upregulation of genes involved in lipid metabolism and a downregulation of genes involved in innate and adaptive immunity, reactive astrogliosis, and chemotaxis. Correspondingly, HPβCD reduced the accumulation of lipid droplets, T

lymphocytes, B lymphocytes, and plasma cells in stroke infarcts. Repeated administration of HPβCD also preserved NeuN immunoreactivity in the striatum and thalamus and c-Fos immunoreactivity in hippocampal regions. Additionally, HPβCD improved recovery through the protection of hippocampal-dependent spatial working memory and reduction of impulsivity. These results indicate that systemic HPβCD treatment following stroke attenuates chronic inflammation and secondary neurodegeneration and prevents post-stroke cognitive decline.

Significance Statement (120 words maximum)

Dementia is a common and debilitating sequela of stroke. Currently, there are no available treatments for post-stroke dementia. Our study shows that lipid metabolism is disrupted in chronic stroke infarcts, which causes an accumulation of uncleared lipid debris and correlates with a chronic inflammatory response. To our knowledge, these substantial changes in lipid homeostasis have not been previously recognized or investigated in the context of ischemic stroke. We also provide a proof of principle that solubilizing and entrapping lipophilic substances using HPβCD could be an effective strategy for treating chronic inflammation after stroke and other CNS injuries. We propose that using HPβCD for the prevention of post-stroke dementia could improve recovery and increase long-term quality of life in stroke sufferers.

Introduction (650 words maximum, including citations)

93 Ischemic stroke is a leading cause of death and disability worldwide (Virani et al., 2020).
94 Of stroke survivors, approximately one-third develop a delayed and progressive form of
95 cognitive decline (Black, 2011); however, there are currently no targeted
96 pharmacological interventions to prevent chronic neurodegeneration after stroke. With
97 an aging global population, there is an increasing need for novel and effective
98 treatments that promote recovery after stroke.
99
100 We previously reported, in a mouse model of post-stroke dementia, that delayed
101 cognitive impairment is caused by a chronic inflammatory response to stroke that is
102 mediated in part by B lymphocytes (Doyle et al., 2015, 2012). In addition to the
103 progressive infiltration of B lymphocytes, T lymphocytes, and IgA+ plasma cells into the
104 infarct in the weeks following stroke, the chronic inflammatory response is also
105 characterized by the production of neurotoxic molecules such as antibodies, cytokines,
106 and degradative enzymes (Zbesko et al., 2021, 2018). These neurotoxic molecules
107 permeate the glial scar and promote chronic inflammation and secondary
108 neurodegeneration in the surrounding parenchyma (Zbesko et al., 2018). Notably, the
109 chronic inflammatory response to stroke has a similar cellular and molecular profile to
110 atherosclerosis. Chronic stroke infarcts contain foamy macrophages, lipid droplets, and
111 intracellular and extracellular cholesterol crystals (Chung et al., 2018). In
112 atherosclerosis, these distinguishing characteristics are caused by overwhelmed lipid
113 processing systems within macrophages, resulting in the recruitment of adaptive
114 immune cells and the production of pro-inflammatory cytokines and degradative
115 enzymes.

116

117 Lipids are principal structural components of the myelin sheath and are major
118 constituents of the human brain (Vance, 2012). Therefore, it is likely that foamy
119 macrophages and cholesterol crystals form in infarcts following ischemic stroke
120 because lipid debris derived from the breakdown of myelin and other cell membranes
121 overwhelms the processing capacity of infiltrating macrophages and resident microglia
122 (Cantuti-Castelvetri et al., 2018). 2-hydroxypropyl-β-cyclodextrin (HPβCD) is a U.S.
123 Food and Drug Administration (FDA)-approved compound that entraps lipids and
124 promotes liver X receptor-mediated transcriptional reprogramming in macrophages to
125 improve cholesterol efflux and incite anti-inflammatory mechanisms (Zimmer et al.,
126 2016). Importantly, HPβCD reduces lipid levels in the lesion following spinal cord injury
127 (Mar et al., 2016) and prevents lipid overload within phagocytic cells in atherosclerosis
128 and Niemann–Pick disease type C (Taylor et al., 2012; Matsuo et al., 2013; Zimmer et
129 al., 2016). Thus, administration of HPβCD is a potential multi-pronged approach for
130 mitigating lipid accumulation in phagocytic cells following ischemic stroke.

131

132 Therefore, the objective of this study was to investigate the efficacy of HPβCD as a
133 prospective treatment for chronic inflammation and delayed cognitive impairment
134 following ischemic stroke. To accomplish this objective, the aims of the study were 2-
135 fold: (1) to characterize the lipidome of chronic stroke infarcts and (2) to determine
136 whether lipid complexation and macrophage reprogramming within infarcts, via the
137 repeated systemic administration of HPβCD, attenuates chronic inflammation and
138 secondary neurodegeneration following stroke. To accomplish these aims, we used the

139 distal middle cerebral artery occlusion + hypoxia mouse model of ischemic stroke in
140 conjunction with immunohistochemistry, RNA-Seq, lipidomics, and behavioral analyses.
141 Our resulting data indicate that, coincident with the substantial accumulation of
142 infiltrating immune cells (Doyle et al., 2015; Zbesko et al., 2021), chronic stroke infarcts
143 amass lipids, including sphingomyelins, cholesterol esters, and sulfatides. We also
144 demonstrate that repeated administration of HPβCD in young adult and aged mice
145 attenuates immune cell and lipid accumulation within chronic stroke infarcts and
146 improves recovery at transcriptional and functional levels. Therefore, HPβCD has the
147 potential to improve stroke recovery and prevent post-stroke dementia in humans.
148

149 **Materials and Methods**

150

151 ***Experimental design and statistical analysis***

152 The study was designed in a manner consistent with STAIR and RIGOR guidelines
153 (Landis et al., 2012; Lapchak et al., 2012; STAIR, 1999). Sample sizes were determined
154 using power analyses based on expected variances and group differences. Allocation of
155 mice into treatment groups was performed randomly, and behavior experiments were
156 performed with the experimenter blind to treatment group. Statistical analyses were
157 performed with Prism 6.0 (GraphPad). Data are presented as the mean ± standard error
158 of mean (SEM). Group sizes, statistical tests, and *p* values for each experiment are
159 reported in **Table 1**. For CBC and lipidomics analyses, normality was assessed using
160 the Kolmogorov—Smirnov test. For all other analyses, data from each individual mouse
161 is presented so the distribution within each group can be visually evaluated; however,

162 the normality was not formally assessed. For GSEA, the normalized enrichment score
163 (NES) is reported. The NES accounts for differences in gene set size and in correlations
164 between gene sets. The NES is based on all dataset permutations to correct for multiple
165 hypothesis testing.
166
167 ***Mice***
168 Young adult (3- to 4-month-old) and aged (17- to 18-month-old) wild-type male
169 C57BL/6J mice (Stock No. 000664) were purchased from The Jackson Laboratory.
170 Mice were housed in a temperature-controlled suite under a 12-hour light–dark regimen,
171 with food and water available *ad libitum*. All procedures met NIH guidelines and were
172 approved by the University of Arizona Institutional Animal Care and Use Committee. At
173 each time point, mice were euthanized by isoflurane anesthesia (JD Medical),
174 exsanguination, and subsequent intracardial perfusion with 0.9% saline. Whole brains
175 or individual brain regions were then removed and either placed in RNAlater (Invitrogen,
176 Cat. No. AM7020) for RNA sequencing analysis; flash frozen in liquid nitrogen for
177 lipidomics analysis; or placed in a 4% paraformaldehyde (PFA) solution for 24 h before
178 being transferred into a 30% sucrose solution for immunostaining analysis. Whole blood
179 collected at the time of euthanasia was either placed directly in heparin-coated tubes for
180 complete blood count analysis or extracted with sodium citrate to separate plasma via
181 centrifugation.
182
183 ***Stroke surgeries***

184 Stroke was induced in mice using the distal middle cerebral artery occlusion + hypoxia
185 (DH) model. The DH stroke model generates a sizable infarct (24% of the ipsilateral
186 hemisphere centered on the somatosensory cortex), has little variability, and has
187 exceptional long-term survivability (Doyle et al., 2012; Nguyen et al., 2016). To induce
188 stroke, we anesthetized animals by isoflurane inhalation and kept them at 37°C
189 throughout the surgical procedure. For all experiments, we injected mice
190 subcutaneously (s.c.) with a single dose of buprenorphine hydrochloride (0.1 mg/kg;
191 Henry Schein) and a single dose of cefazolin antibiotic (25 mg/kg; Sigma-Aldrich)
192 dissolved in sterile saline. Following pre-operative preparation, an incision was made to
193 expose the right temporoparietal skull between the orbit and the ear. Under an
194 operating microscope, a small hole was made with a high-speed microdrill through the
195 outer surface of the semi-translucent skull over the visually identified middle cerebral
196 artery (MCA) at the level of the parietal cerebral artery. Permanent occlusion of the
197 MCA was performed by electrocoagulation with a small vessel cauterizer (Bovie Medical
198 Corporation). Surgical wounds were closed using Surgi-lock 2oc tissue adhesive
199 (Meridian Animal Health). We then immediately transferred mice to a hypoxia chamber
200 (Coy Laboratory Products) containing 9% oxygen and 91% nitrogen for 45 min.
201 Sustained-release buprenorphine (Bup-SR, 1 mg/kg s.c.; ZooPharm) was administered
202 24 h after surgery as post-operative analgesia.
203
204 ***Magnetic resonance imaging (MRI)***
205 Infarct volume was assessed by magnetic resonance imaging (MRI) 24 h after stroke
206 using a Bruker Biospec 70/20 7.0T scanner with ParaVision-360.2.0 software and a 4-

207 channel phase array mouse coil (Bruker Biospin GmbH, Germany). Mice were placed in
208 a cradle equipped with a stereotaxic frame, an integrated heating system to maintain
209 body temperature at 37±1°C, and a pressure probe to monitor respiration. During MRI
210 acquisition, anesthesia was maintained by inhalation of 1.5-3% isoflurane.
211 High-resolution structural images were acquired using a T_2-weighted RARE multi-echo
212 Bruker pulse sequence with the following parameters: repetition time (*TR*) = 2000 ms;
213 flip angle = 180°; RARE factor = 12; matrix size = 128 x 128; averages = 2; field of view
214 (FOV) = 1.92 cm x 1.92 cm; slice thickness = 0.8 mm; number of slices = 15; acquisition
215 time = 8 min 53 s. Infarcts and hemispheric cross sections were manually delineated on
216 T_2-weighted images using Mango v4.1.
217
218 ***Drug treatment***
219 We injected HPβCD or vehicle s.c. three times per week, beginning 7 days after stroke
220 surgery, for 6 weeks until euthanasia at 7 weeks after stroke. Mice in the treatment
221 group received 2-hydroxypropyl-β-cyclodextrin powder (Sigma-Aldrich, Cat. No. H-107)
222 dissolved in sterile phosphate-buffered saline (PBS) at a dose of 4 g HPβCD/kg body
223 weight. Mice in the vehicle control group received 300 µL sterile PBS.
224
225 ***Immunostaining***
226 Coronal brain sections (40 µm) were collected using a freezing Microm HM 450 sliding
227 microtome (Thermo Fisher Scientific) and stored in cryoprotectant medium at –20°C
228 until processing. Immunostaining was performed on free-floating brain sections using
229 standard protocols (Doyle et al., 2015; Nguyen et al., 2016; Zbesko et al., 2018).

230 Primary antibodies against neuronal nuclei (NeuN; 1:500; Millipore Sigma, Cat. No.
231 MAB377; RRID:AB_2298772), c-Fos (1:2000; Abcam, Cat. No. ab190289;
232 RRID:AB_2737414), CD3ε (1:1000; BD Biosciences, Cat. No. 550277;
233 RRID:AB_393573), B220/CD45R (1:500; BD Biosciences, Cat. No. 553085;
234 RRID:AB_394615), immunoglobulin A (IgA; 1:1000; BioLegend, Cat. No. 407004;
235 RRID:AB_315079), and CD138 (Syndecan-1; 1:200; BioLegend, Cat. No. 142514;
236 RRID:AB_2562198) were used in conjunction with the appropriate secondary antibody
237 and visualized using the VECTASTAIN Elite ABC Reagent, Peroxidase, R.T.U. (Vector
238 Laboratories, Cat. No. PK-7100) and Vector DAB Substrate (3,3'-diaminobenzidine) Kit
239 (Vector Laboratories, Cat. No. SK-4100). Secondary antibodies were diluted 1:400 for
240 biotinylated horse anti-mouse IgG (Vector Laboratories, Cat. No. BA-2000;
241 RRID:AB_2313581), biotinylated goat anti-hamster IgG (Vector Laboratories, Cat. No.
242 BA-9100; RRID:AB_2336137), and biotinylated rabbit anti-rat IgG (Vector Laboratories,
243 Cat. No. BA-4000; RRID:AB_2336206). Sections were imaged using a Keyence BZ-
244 X700 digital microscope with phase contrast, light, and fluorescence capabilities.
245
246 ***Oil Red O staining***
247 Frozen tissue sections were mounted on slides and allowed to dry. Mounted sections
248 were dehydrated in 100% propylene glycol for 5 min and then stained with Oil Red O
249 (ORO) for 10 min (Abcam, Cat. No. ab150678). The sections were then differentiated in
250 85% propylene glycol for 3 min and rinsed with distilled water three times. Coverslips
251 were applied to all slides using an aqueous mounting medium (Vector Laboratories,

252 Cat. No. H-1400). Stained sections were imaged with a Keyence BZ-X700 digital
253 microscope.
254
255 ***Alcian blue staining***
256 Frozen tissue sections were mounted on slides and allowed to dry. Slides were
257 immersed in eosin (VWR, Cat. No. 95057-848) and then rinsed eight times in PBS.
258 Slides were incubated in 3% acetic acid (pH 2.5) for 3 min and then placed in a solution
259 of 1% w/v Alcian blue in 3% acetic acid (pH 2.5) for 30 min (EMD Millipore, Cat. No.
260 TMS-010-C). Slides were then rinsed in 3% acetic acid and allowed to dry overnight.
261 Slides were cleared in xylene and preserved with Entellan mounting medium (EMD
262 Millipore, Cat. No. 14802) and coverslips. Stained sections were imaged with a Keyence
263 BZ-X700 digital microscope.
264
265 ***Quantification of staining***
266 To quantify the amount of positive staining for CD3ε, B220, Oil Red O, and Alcian blue,
267 we used Fiji (Schindelin et al., 2012). The 'Colour Deconvolution' function was used to
268 separate color channels in images of Alcian blue staining. We then converted all
269 stitched images to 8-bit and traced the stroke infarct using the 'Polygon selections' tool.
270 We applied a threshold of positive staining to each image and measured the pixel area
271 of positive staining within the selected region. To quantify IgA and CD138, we utilized
272 the 'Cell Counter' plugin to manually count the number of positive cells within the stroke
273 infarct. To quantify NeuN and c-Fos immunoreactivity in vehicle- and HPβCD-treated
274 mice, we used Fiji to perform global thresholding in conjunction with a watershed

275 algorithm on the ipsilateral side and equivalent region in the contralateral hemisphere.
276 Fields covering the selected regions were analyzed at bregma +0.38 mm and −1.46 mm
277 (NeuN) or −1.82 mm (c-Fos) using a 20× objective lens. We also measured
278 hippocampal area in images captured with a 2× objective lens by tracing the
279 hippocampus with the 'Polygon selections' tool in Fiji.
280
281 ***RNA sequencing and data analysis***
282 Infarcts were visually identified and dissected using forceps and a razor blade.
283 Following infarct removal, adjacent peri-infarct regions were dissected. Corresponding
284 regions in the contralateral hemisphere were also dissected. Fresh brain tissue
285 collected from vehicle- and HPβCD-treated mice was immersed in RNAlater (Invitrogen,
286 Cat. No. AM7020) and delivered to the University of Arizona Genetics Core. Samples
287 were assessed for quality with an Advanced Analytics Fragment Analyzer (High
288 Sensitivity RNA Analysis Kit, Cat. No. DNF-491/User Guide DNF-491-2014AUG13) and
289 quantity with a Qubit RNA HS Assay Kit (Cat. No. Q32852). Given satisfactory quality
290 (RNA integrity number >8) and quantity, samples were used for library construction with
291 the TruSeq Stranded mRNA Library Prep Kit from Illumina (Cat. No. 20020595), as well
292 as the KAPA Dual-Indexed Adapter Kit from Roche (Cat. No. 8278555702). Upon
293 completion of library construction, samples were assessed for quality and average
294 fragment size with the Advanced Analytics Fragment Analyzer (High Sensitivity NGS
295 Analysis Kit, Cat. No. DNF-846/User Guide DNF-486-2014MAR10). Quantity was
296 assessed with an Illumina Universal Adaptor-specific qPCR kit from KAPA Biosystems
297 (KAPA Library Quantification Kit for Illumina NGS, Cat. No. KK4824/KAPA Library

298 Quantification Technical Guide – AUG2014). Following the final library quality control,
299 samples were equimolar-pooled and clustered for paired-end sequencing on the
300 Illumina NextSeq500 machine to generate 75 bp reads. The sequencing run was
301 performed using Illumina NextSeq500 run chemistry (NextSeq500/550 High Output v2
302 Kit 150 cycles, Cat. No. FC-404-2002). Sequencing data is publicly available at the
303 National Center for Biotechnology Information through Gene Expression Omnibus
304 accession numbers: GSE173544 and GSE173715. For data analysis, the resulting
305 sequences were demultiplexed using bcl2fastq v2.19 (Illumina) and trimmed of their
306 indexing adaptors using Trimmomatic v0.32 (Bolger, Lohse, & Usadel, 2014). The
307 trimmed reads were aligned to the GRCm38 reference genome using STAR v2.5.2b
308 (Dobin et al., 2013). Gene expression was calculated using the htseq-count function of
309 the HTSeq python tool (Anders, Pyl, & Huber, 2015). Genes were annotated using the
310 BioMart database. Differential expression analysis of count tables was performed using
311 DESeq2 (Love, Huber, & Anders, 2014). Gene set enrichment analysis (GSEA) was
312 performed on all significant differentially expressed genes (false discovery rate [FDR]-
313 adjusted $p < 0.05$) using a database of Gene Ontology (GO) terms for biological
314 processes. Enrichment maps were constructed from GO terms using the Enrichment
315 Map Cytoscape application (Merico, Isserlin, Stueker, Emili, & Bader, 2010). Minimal
316 editing, such as repositioning of nodes and removal of repetitive gene-sets, was
317 performed to optimize the map layout. Pathway analysis was performed on all
318 differentially expressed genes using Ingenuity Pathway Analysis v01-13 (IPA).
319
320 ***Targeted lipidomics analysis (LIPID MAPS Lipidomics Core)***

321 Fresh brain tissue dissected from vehicle- and HPβCD-treated mice was flash frozen
322 and delivered to the LIPID MAPS Lipidomics Core at the University of California, San
323 Diego. Upon arrival, each sample underwent lipid extraction and quality control
324 analyses. The comprehensive sphingolipid panel and cholesterol ester panel were
325 independently performed using established protocols (Quehenberger et al., 2010).
326
327 ***Flow cytometry***
328 To assess peripheral immune cell populations, spleens were extracted after transcardial
329 perfusion with 0.9% saline. Each spleen was crushed in 1 mL ammonium–chloride–
330 potassium RBC lysing buffer and resuspended in 1 mL complete DMEM. For cell
331 staining, fluorophore-conjugated monoclonal antibodies specific for CD4 (RM4-5), CD8α
332 (53-6.7), and TCRβ (H57-597) were obtained from BioLegend. Monoclonal antibodies
333 specific for CD19 (6D5) and GL7 (GL7) were purchased from BD Pharmingen.
334 Antibodies against IgG1 (RMG1-1) and IgA (RMA-1) were obtained from BioLegend.
335 For intranuclear staining, buffers from a Foxp3 Staining Buffer Set (eBioscience) were
336 used to stain antibodies recognizing Foxp3 (FJK-16s, eBioscience). Cells were run on a
337 BD LSR II flow cytometer (BD Biosciences) and analyses were performed with FlowJo
338 v10.7 for Windows (Tree Star).
339
340 ***Y-maze spontaneous alternation behavior test***
341 Spatial working memory was assessed with the spontaneous alternation behavior (SAB)
342 paradigm. Testing occurred in a Y-shaped maze consisting of two symmetrical arms
343 and one longer arm arranged at 120° angles (symmetrical arms: 7.5 cm wide, 37.0 cm

344 long, 12.5 cm high; longer arm: 7.5 cm wide, 42.0 cm long, 12.5 cm high). Mice were
345 placed at the end of the longest arm and allowed to freely explore the three arms in a 5
346 min trial, as described previously (Doyle et al., 2015). The number of arm entries and
347 the number of correct alternations were recorded by an ANY-maze behavioral video
348 tracking software (Stoelting, Co.). An entry was recorded when all four limbs of the
349 mouse were within an arm.
350
351 ***Light/dark transition test***
352 The light/dark box arena consisted of a Plexiglas box (40 cm wide, 40 cm long, 35 cm
353 high) divided by a small underpass into two equally sized compartments: a brightly
354 illuminated zone (390 lux) and a covered dark zone (2 lux). Prior to the test, animals
355 were habituated to the dark for 30 min. Mice were then placed in the dark chamber of
356 the arena and allowed to move freely between the two chambers for 10 min. The time
357 spent in each chamber, the latency to exit the dark chamber, and the total number of
358 transitions were recorded by an ANY-maze behavioral video tracking software
359 (Stoelting, Co.).
360
361 **Results**
362
363 ***Lipid composition of chronic stroke infarcts in young adult mice***
364 Prior to evaluating the lipid composition of chronic stroke infarcts, we performed T_2-
365 weighted MRI on young adult mice 24 hours after stroke to visualize the acute area of
366 infarction generated by the distal middle cerebral artery occlusion + hypoxia (DH) stroke

367 model. As previously shown, infarcts were reliably centered on the somatosensory
368 cortex and included a portion of the M1 region of the primary motor cortex (Doyle et al.,
369 2012). Notably, infarcts did not extend to the hippocampus **(Fig. 1A)**.
370
371 We previously reported that, similar to atherogenesis, chronic stroke infarcts
372 accumulate foamy macrophages, cholesterol crystals, and lipid droplets, which results
373 in the upregulation of osteopontin, MMPs, and pro-inflammatory cytokines (Chung et al.,
374 2018). To further evaluate the similarities between the pathophysiology of chronic stroke
375 infarcts and atherosclerosis, we evaluated lipid droplet accumulation in chronic stroke
376 infarcts. In the context of atherosclerosis, macrophages frequently become foamy in
377 appearance due to the accumulation of cholesterol esters stored within lipid droplets. In
378 addition to their role as storage containers within foamy macrophages, lipid droplets
379 also contribute directly and indirectly to the pathology of progressing atherosclerotic
380 plaques (Goldberg et al., 2018). To visualize lipid droplets in chronic stroke infarcts, we
381 performed Oil Red O (ORO) staining on brain sections from young adult mice at 7
382 weeks after stroke. ORO staining revealed more intracellular lipid droplets in the infarcts
383 compared to the contralateral cortices **(Fig. 1B)**. These findings provide additional
384 evidence that chronic stroke infarcts and atherosclerotic plaques share several similar
385 pathophysiological features.
386
387 To assess whether lipid accumulation in chronic stroke infarcts is derived from myelin
388 breakdown, we performed Alcian blue staining on brain sections from young adult mice
389 at 7 weeks post-stroke. Alcian blue stains for sulfatide, a major constituent of CNS

390 myelin. Importantly, sulfatide was recently identified as a myelin-associated inhibitor of
391 neurite outgrowth (Winzeler et al., 2011). Chronic stroke infarcts contained an
392 abundance of sulfatides at 7 weeks after stroke **(Fig. 1C)**, indicating that phagocytic
393 cells, including resident microglia and infiltrating macrophages, are strained in their
394 capacity to process and eliminate myelin lipid debris for at least 7 weeks after stroke.
395
396 To further evaluate myelin-derived lipids in chronic stroke infarcts, we performed a
397 targeted lipidomics analysis to assess sphingomyelin levels within infarcts compared to
398 contralateral cortices of young adult mice at 7 weeks after stroke. Importantly,
399 sphingomyelins play a central role in the structure of myelin, constituting 4% of myelin
400 lipid content. The accumulation of sphingomyelin is a hallmark of Niemann–Pick
401 disease and leads to changes in the plasma membrane that promote
402 neurodegeneration (Mar et al., 2016). Sphingomyelins are also involved in signal
403 transduction pathways and in the regulation of cholesterol and protein trafficking to
404 myelin (Poitelon, Kopec, & Belin, 2020). In addition to their role in myelin architecture,
405 sphingomyelins are involved in microglial activation and inflammation (Fitzner et al.,
406 2020; Yang et al., 2020). Chronic stroke infarcts were enriched in sphingomyelins 7
407 weeks after stroke **(Fig. 1D),** indicating a pronounced dysregulation of myelin lipid
408 homeostasis in chronic stroke infarcts of young adult mice.
409
410 ***Lipid composition of chronic stroke infarcts in aged mice***
411 Stroke remains the leading cause of long-term disability in people over the age of 65
412 (Virani et al., 2020). Therefore, we used aged (18-month-old) mice to further

413 characterize the lipid composition of chronic stroke infarcts. First, to corroborate our
414 observations in young adult mice, we used ORO to stain for lipid droplets in brain
415 sections collected from aged mice at 7 weeks after stroke. We observed significantly
416 more intracellular lipid droplets in infarcts compared to contralateral cortices **(Fig. 2A)**.
417 In addition, Alcian blue staining revealed that chronic stroke infarcts in aged mice are
418 also characterized by an abundance of sulfatides when compared with contralateral
419 cortices at 7 weeks after stroke **(Fig. 2B)**. When comparing these results with those
420 obtained in young adult mice, we see that aged mice have a comparable accumulation
421 of lipid droplets and sulfatides at 7 weeks after stroke. Together, these results indicate
422 that young adult and aged mice share similar impediments in the clearance of myelin
423 lipid debris.
424
425 Cholesterol is esterified prior to storage in cytoplasmic lipid droplets to prevent free
426 cholesterol-associated cell toxicity (Ghosh et al., 2010). Therefore, we evaluated the
427 composition of cholesterol esters stored in lipid droplets via a second targeted
428 lipidomics analysis. For this analysis, we again compared infarcts at 7 weeks after
429 stroke to equivalent regions of the contralateral cortex. All quantified cholesterol ester
430 species were significantly elevated in infarcts of aged mice at 7 weeks after stroke
431 compared to contralateral cortices **(Fig. 2C)**.
432
433 ***Transcriptome of the chronic stroke infarct in young adult mice***
434 To systematically characterize the chronic stroke infarct transcriptome, we conducted
435 bulk RNA sequencing (RNA-Seq) on infarcts collected at 7 weeks after stroke and

436 compared them to equivalent regions of the contralateral cortex **(Fig. 3A)**. As expected,
437 differential expression (DE) analysis revealed marked differences between infarcts and
438 contralateral cortices. The resultant volcano plot illustrates the distribution of 3,930
439 upregulated and 2,869 downregulated genes **(Fig. 3B)**. The most significantly
440 upregulated genes, including *Lpl*, *Spp1*, *Cd36*, *Mmp2*, and *Mmp19*, and the most highly
441 enriched genes, including *Cd5l*, *Mmp3*, *Mmp12*, and *Mmp13*, indicate a pronounced
442 disturbance in lipid homeostasis in infarcts at 7 weeks after stroke. Importantly, Zhu et
443 al. (2017) similarly identified *Cd5l*, *Lpl*, and *Cd36* as highly expressed genes in foamy
444 macrophages after spinal cord injury (SCI) (Zhu et al., 2017).
445
446 Correspondingly, chronic stroke infarcts were also characterized by an upregulation of
447 TLRs, including *Tlr1*, *Tlr2*, and *Tlr4*, and scavenger receptors, including *Scarb2*, *Cd68*,
448 *Msr1*, and *Cxcl16*. These genes are implicated in the induction and progression of
449 atherosclerosis; importantly, these scavenger receptors mediate the uptake of oxLDL
450 into macrophages and promote their differentiation into foam cells (Aslanian & Charo,
451 2006; Febbraio, Hajjar, & Silverstein, 2001; Park, 2014; Rahaman et al., 2006; Zeibig et
452 al., 2019). Dysregulated lipid homeostasis within infarcts is further evidenced by the
453 upregulation of genes involved in lipid metabolism: *Npc1*, *Npc2*, *Lamp1*, *Ffar1*, *Pparg*,
454 *Apoe*, *Trem2*, and *Abca1* **(Fig. 3C)**.
455
456 In addition to alterations in lipid metabolism, the transcriptome also revealed a signature
457 of chronic inflammation at 7 weeks after stroke. For instance, activation of the innate
458 immune response is indicated by the upregulation of genes involved in complement

459 cascade activation, including *C1s1*, *C3ar1*, and *C3*, and in phagocytosis, including
460 *Tmem119*, *Hexb*, *Nlrp3*, *Ctsb*, and *Myd88*. Further, upregulated genes included *Gfap*,
461 *Lcn2*, and *Serpina3n*, which have been validated as specific markers of reactive
462 astrogliosis in ischemic stroke and LPS-induced neuroinflammation (Zamanian et al.,
463 2012) **(Fig. 3C)**. Together, these genes signify the activation of innate immune cells,
464 including infiltrating macrophages, resident microglia, and astrocytes.
465
466 Additionally, activation of the adaptive immune system is indicated by the upregulation
467 of genes associated with T lymphocytes, including *Cd2*, *Cd3e*, *Gzma*, *Gzmb*, and *Prf1*;
468 B lymphocytes, including *CD19*, *Cd79a*, and *Blnk*; and antibody-producing plasma cells,
469 including *Sdc1* and *Jchain* **(Fig. 3C)**. These perturbations in innate and adaptive
470 immunity demonstrate that chronic inflammation persists in infarcts for at least 7 weeks
471 after stroke, as we have shown previously (Chung et al., 2018; Doyle et al., 2015;
472 Zbesko et al., 2021).
473
474 In conjunction with the upregulation of genes involved in chronic inflammation and lipid
475 metabolism, the DE analysis revealed a downregulation of genes involved in neuronal
476 structure and function. Specifically, the neurofilament subunits *Nefh*, *Nefm*, and *Nefl*
477 were downregulated, which indicates persistent disruption or absence of neuronal
478 cytoskeletons in infarcts at 7 weeks after stroke **(Fig. 3C)**.
479
480 We then used IPA software to define upstream regulators and identify altered biological
481 processes based on DE analysis. Differentially expressed genes were associated with

482 the following upregulated biological processes: (i) atherosclerosis signaling, (ii) IL-1
483 signaling, (iii) inflammasome pathway, (iv) eicosanoid signaling, (v) B cell receptor
484 (BCR) signaling, and (vi) phospholipases, along with others. In contrast, differentially
485 expressed genes were associated with the following downregulated biological
486 processes: (i) calcium signaling, (ii) glutamate receptor signaling, and (iii) synaptic long-
487 term potentiation **(Fig. 4A, B)**. These altered biological processes indicate that the
488 stroke infarct transcriptome is characterized by chronic inflammation, dysregulated lipid
489 metabolism, and impaired or absent neuronal function at 7 weeks after stroke. In
490 addition, IPA identified lipid metabolic upstream regulators such as cholesterol,
491 phospholipids, and LDL, as well as immunological upstream regulators such as MYD88,
492 IL18, CD3, IL1B, TLR4, and TNF **(Fig. 4C)**.
493
494 ***HPβCD attenuates the chronic inflammatory response to stroke in young adult***
495 ***mice***
496 To investigate the role of lipid metabolism in the chronic inflammatory response to
497 stroke, we administered subcutaneous injections of 4 g/kg HPβCD or vehicle control to
498 young adult mice triweekly (Monday, Wednesday, and Friday) for 6 weeks, beginning 1
499 week after stroke **(Fig. 5A)**. We performed immunostaining on vehicle- and HPβCD-
500 treated brain sections at 7 weeks post-stroke. These analyses revealed substantially
501 fewer B220+ B lymphocytes, CD3ε+ T lymphocytes, and CD138+ and IgA+ antibody-
502 producing plasma cells in infarcts of HPβCD-treated mice than in infarcts of vehicle-
503 injected mice. In addition, ORO staining revealed that infarcts of HPβCD-treated mice
504 had fewer lipid droplets than those of vehicle-injected mice **(Fig. 5B)**. These differences

505 indicate that repeated administration of HPβCD following stroke attenuates chronic
506 inflammation and lipid droplet formation in young adult mice. Conversely, the
507 accumulation of sulfatides in infarcts of vehicle- and HPβCD-treated mice was
508 comparable **(Fig. 5B)**, suggesting that HPβCD does not aid in the clearance of
509 sulfatides.
510
511 ***HPβCD attenuates the chronic inflammatory response to stroke in aged mice***
512 Stroke prevalence and mortality rates increase with advancing age in both males and
513 females (Virani et al., 2020). Therefore, to address age as a biological variable, we
514 performed immunohistochemistry and bulk RNA-Seq analyses on aged (18-month-old)
515 mice treated with HPβCD using the same treatment regimen as in young adult mice
516 (HPβCD or vehicle control three times per week for 6 weeks) **(Fig. 6A)**. We discovered
517 that, consistent with young adult mice, aged mice had substantially fewer B220+ B
518 lymphocytes, CD3ε+ T lymphocytes, and IgA+ antibody-producing plasma cells in their
519 infarcts following repeated administration of HPβCD. In addition, ORO staining revealed
520 that infarcts of HPβCD-treated mice had significantly less lipid droplet accumulation
521 than vehicle-injected mice at 7 weeks after stroke **(Fig. 6B)**. These results demonstrate
522 that young adult and aged mice similarly exhibit attenuated lipid droplet and immune cell
523 accumulation in chronic stroke infarcts following repeated administration of HPβCD.
524 However, the accumulation of sulfatides in vehicle- and HPβCD-treated aged mice was
525 comparable **(Fig. 6B)**, reinforcing that HPβCD does not aid in the clearance of
526 sulfatides.
527

528 ***HPβCD does not alter peripheral immune cell populations in the blood or spleens***
529 ***of aged mice after stroke***
530 The spleen, a secondary lymphoid organ, is a major reservoir of immune cells and a
531 focal point for the immune response to tissue injury. In response to ischemic stroke,
532 splenocytes enter into systemic circulation and migrate to the brain, exacerbating
533 neurodegeneration (Seifert et al., 2012). To determine the effect of HPβCD on
534 peripheral immune cell populations, we used flow cytometry to quantify splenic cell
535 populations. There were no significant differences in CD19+ B lymphocytes or GL-7+
536 germinal center B lymphocytes **(Fig. 7A, B),** or in IgG1 and IgA isotypes **(Fig. 7C)**,
537 between the spleens of vehicle- and HPβCD-treated mice at 7 weeks after stroke. The
538 CD4+ T lymphocyte, CD8+ T lymphocyte, and Treg populations were also not
539 significantly altered by repeated HPβCD administration **(Fig. 7D, E)**. These results
540 demonstrate that splenic cell populations in HPβCD-treated aged mice are not
541 significantly altered in comparison to those of vehicle-injected mice.
542
543 A complete blood count analysis on blood collected from vehicle- and HPβCD-treated
544 aged mice at 7 weeks after stroke also revealed no significant differences in the number
545 of circulating white blood cells, neutrophils, lymphocytes, monocytes, eosinophils, or
546 basophils **(Fig. 7F)**. Together, the flow cytometry and complete blood count analyses
547 indicate that, while there were substantially fewer immune cells in infarcts of HPβCD-
548 treated aged mice than in those of vehicle-injected mice at 7 weeks after stroke **(Fig.**
549 **6B)**, repeated systemic HPβCD administration does not significantly alter circulating or
550 splenic immune cell populations in aged mice.

551

552 ***HPβCD promotes lipid metabolism and attenuates inflammation in infarcts of***

553 ***aged mice after stroke***

554 We systematically characterized the transcriptomes of stroke infarcts in vehicle- and

555 HPβCD-treated aged mice by performing bulk RNA-Seq on infarcted brain tissue

556 collected 7 weeks after stroke **(Fig. 8A)**. As shown in the volcano and MA plots, the DE

557 analysis revealed 991 upregulated genes and 1,876 downregulated genes **(Fig. 8B, C)**.

558 HPβCD treatment upregulated intracellular cholesterol transporters, lipoproteins, and

559 lipoprotein receptors, such as *Npc1*, *Npc2*, *Apoe*, *Trem2*, *Abca1*, *Vldlr*, and *Hdlbp*, and

560 downregulated *Ffar1*, *Lrpb1*, and *Dgkb* **(Fig. 8D, E)**. These alterations in lipid

561 metabolism suggest that HPβCD aids in the restoration of lipid homeostasis by 7 weeks

562 after stroke. In addition, the DE analysis revealed a downregulation of genes involved in

563 chemotaxis, including *Cx3cr1*, *Cxcl5*, and *Ccr6*, and innate and adaptive immune

564 responses, including *Mmd2*, *Mzb1*, *Btla*, *Jchain*, and *Igkv5-48*. Correspondingly, there

565 was an upregulation of anti-inflammatory genes, such as *Tgfb1*, *Tgfb2*, *P2ry2*, and

566 *Il18bp* **(Fig. 8D)**. These results indicate that HPβCD attenuates the chronic

567 inflammatory response to stroke in aged mice.

568

569 We also identified alterations in genes involved in the composition of membranes,

570 including *Olig1*, *Pmp22*, *Mal2*, *Rftn1*, and *Plp*. These alterations suggest that HPβCD

571 modifies lipid rafts and cell membranes by 7 weeks after stroke. Genes involved in

572 angiogenesis were also upregulated, including *Nrp1*, *Vash2*, *Hpse*, *Vegfc*, *Vegfd*, and

573 *Ndnf* **(Fig. 8D)**. In addition, enrichment maps constructed from GO terms revealed an

574 upregulation of lipid metabolism, angiogenesis, and collagen synthesis pathways and a
575 downregulation of immune response pathways **(Fig. 9A)**. These results indicate that
576 HPβCD treatment promotes lipid metabolism and angiogenesis and dampens chronic
577 inflammation in infarcts of aged mice at 7 weeks after stroke.
578
579 Next, we performed genome-wide expression analysis of the RNA-Seq data using
580 GSEA, which revealed significant enrichment of various biological processes in infarcts
581 of HPβCD-treated aged mice, including (i) collagen formation, (ii) regulation of
582 angiogenesis, (iii) lipid catabolic process, (iv) regulation of autophagy, and (v) regulation
583 of apoptotic process. Conversely, GSEA identified biological processes more enriched
584 in infarcts of vehicle-injected mice compared to HPβCD-treated mice, including (i) innate
585 immune response, (ii) adaptive immune response, (iii) immunoglobulin production, (iv)
586 phagocytosis, engulfment, and (v) complement activation, classical pathway **(Fig. 9B)**.
587 These results further indicate that infarcts of vehicle-injected mice are defined by
588 increased innate and adaptive immune responses, whereas those of HPβCD-treated
589 mice are defined by increased angiogenic and lipid metabolic processes.
590
591 ***Transcriptome of the peri-infarct region in aged mice at 7 weeks after stroke***
592 Prior to assessing the impact of repeated HPβCD administration on the peri-infarct
593 region of the brain, we first compared the transcriptome of the peri-infarct region to the
594 equivalent region of the contralateral hemisphere in aged mice at 7 weeks after stroke
595 **(Fig. 10A)**. The peri-infarct region was characterized by 3,910 differentially expressed
596 genes **(Fig. 10B, C)**. Of these, 2,123 were upregulated, many of which were also

597 upregulated in infarcts at 7 weeks after stroke **(Fig. 3C)**. For instance, the infarct and
598 peri-infarct regions were both defined by the upregulation of degradative enzymes,
599 including *Mmp2*, *Mmp3*, and *Mmp8*; TLRs, including *Tlr1*, *Tlr2*, and *Tlr4*; and scavenger
600 receptors, including *Cd36*, *Cd68*, and *Cxcl16*. Additionally, peri-infarct regions were
601 characterized by specific markers of reactive astrogliosis, including *Gfap*, *Lcn2*, and
602 *Serpina3n* **(Fig. 10D)**.
603
604 Similar to the transcriptome of the infarct at 7 weeks after stroke, the transcriptome of
605 the peri-infarct region was primarily defined by genes involved in chronic inflammation
606 and dysregulated lipid metabolism. The upregulation of *Lpl*, *Lrp2*, *Ch25h*, *Apoe*, *Trem2*,
607 and *Abca1* signifies a divergence from lipid homeostasis. Moreover, *Ldlr* was
608 downregulated, which implies impaired lipoprotein and lipid metabolism (Go & Mani,
609 2012). In addition, genes involved in complement cascade activation (including *C1s1*,
610 *C3ar1*, and *C3*) and phagocytosis (including *Tmem119*, *Hexb*, *Nlrp3*, and *Mmd2*) were
611 upregulated in peri-infarct regions. These alterations in innate immunity coincided with
612 corresponding perturbations in adaptive immunity. The upregulation of *Cd3d*, *Cd3e*,
613 *Cd3g*, *Blnk*, *Sdc1* and *Jchain* suggests that chronic inflammation persists in peri-infarct
614 regions for at least 7 weeks after stroke **(Fig. 10D)**.
615
616 Conversely, the DE analysis revealed that 1,787 genes were downregulated in peri-
617 infarct regions compared to equivalent regions of the contralateral hemisphere. These
618 genes were primarily involved in mitochondrial respiration and neuronal function.
619 Specifically, genes involved in mitochondrial fission and respiration, including *Cyc1*,

620 *Coa3*, *Cox5a*, and *Mff*, and the neurofilament subunits *Nefh*, *Nefm*, and *Nefl*, were
621 downregulated **(Fig. 10D)**. Together, these results demonstrate that the transcriptome
622 of the peri-infarct region is characterized by the upregulation of genes involved in
623 inflammation and lipid metabolism and the downregulation of genes involved in
624 mitochondrial respiration and neuronal function.
625
626 Next, we performed genome-wide expression analysis of the RNA-Seq data using
627 GSEA. GSEA revealed significant enrichment of various biological processes in peri-
628 infarct regions of aged mice, including (i) macrophage activation, (ii) cytokine
629 production, (iii) BCR signaling pathway, (iv) lipoprotein metabolism, and (v)
630 phagocytosis. In contrast, GSEA identified biological processes more significantly
631 enriched in equivalent regions of the contralateral hemisphere, including (i) synaptic
632 vesicle localization, (ii) mitochondrion organization, (iii) neurotransmitter secretion, (iv)
633 myelin sheath, and (v) mitochondrial transport **(Fig. 11)**. These results further indicate
634 that peri-infarct regions are defined by chronic inflammation and dysregulated lipid
635 metabolism, whereas equivalent regions of the contralateral hemisphere are defined by
636 intact neuronal function.
637
638 ***HPβCD attenuates inflammation and increases transcripts associated with***
639 ***neuronal function in peri-infarct regions of aged mice after stroke***
640 To evaluate the impact of HPβCD treatment on the transcriptome of the peri-infarct
641 region, we performed bulk RNA-Seq on brain tissue collected 7 weeks after stroke. For
642 this analysis, we compared the peri-infarct regions of vehicle- and HPβCD-treated aged

643 mice **(Fig. 12A)**. The peri-infarct region of HPβCD-treated mice was characterized by
644 5,385 differentially expressed genes **(Fig. 12B, C)**. The DE analysis revealed that
645 specific markers of reactive astrogliosis, including *Gfap*, *Serpina3n*, and *Stat3*, were
646 downregulated following HPβCD treatment. The peri-infarct region of HPβCD-treated
647 mice was also characterized by the downregulation of multiple degradative enzymes,
648 including *Mmp2*, *Mmp8*, and *Mmp14*; chemokine receptors, including *Ccr2*, *Cx3cr1*; and
649 *Cxcr4*, and scavenger receptors, including *Cd36*, *Cd68*, and *Cxcl16* **(Fig. 12D)**.
650
651 In addition, the transcriptomic analysis demonstrated a restoration of lipid homeostasis
652 in peri-infarct regions of HPβCD-treated mice compared to vehicle-injected mice, as
653 evidenced by the downregulation of *Lipa*, *Apoe*, *Lamp1*, *Npc1*, and *Npc2* and
654 upregulation of *Nceh1* and *Ldlr*. A reduction in the innate immune response (identified
655 by *Tlr4*, *Csf1*, and *C2*) and in the adaptive immune response (identified by *Sdc1*,
656 *Gsdmd*, and *Cd1d1*) characterized peri-infarct regions of HPβCD-treated mice **(Fig.
657 12D)**; these alterations are consistent with the attenuated chronic inflammation that
658 characterized infarcts of the HPβCD-treated aged mice **(Fig. 8D)**. These results
659 demonstrate that HPβCD treatment after stroke attenuates chronic inflammation and
660 promotes lipid metabolism in peri-infarct regions of aged mice. Additionally, the DE
661 analysis revealed an upregulation of genes involved in myelin sheath structural integrity,
662 such as *Ina*, *Omg*, and *Nefl*, and synaptic plasticity and neuroplasticity, such as *Syn1*,
663 *Bdnf*, *Nrg1*, *Negr1*, and *Nsg1* **(Fig. 12D)**. These results suggest that HPβCD treatment
664 improves the structure and function of neurons in peri-infarct regions of aged mice after
665 stroke.

666

667 Next, we performed genome-wide expression analysis of the RNA-Seq data using
668 GSEA, which revealed a significant enrichment of various biological processes in peri-
669 infarct regions of HPβCD-treated aged mice, including (i) synaptic vesicle localization,
670 (ii) neuron projection membrane, (iii) dendritic spine organization, (iv) myelin sheath,
671 and (v) regulation of axonogenesis. Conversely, biological processes more significantly
672 enriched in vehicle-injected mice than in HPβCD-treated mice included (i) macrophage
673 activation, (ii) binding and uptake of ligands by scavenger receptors, (iii) cytokine
674 production, (iv) lipid droplet, (v) lymphocyte mediated immunity, and (vi) lipid catabolic
675 process **(Fig. 13)**. These results demonstrate that peri-infarct regions of HPβCD-treated
676 aged mice are characterized by enhanced membrane integrity and reduced
677 inflammation compared to vehicle-injected aged mice.

678

679 ***HPβCD attenuates neurodegeneration and improves recovery in aged mice after***
680 ***stroke***

681 To assess behavioral outcomes following HPβCD treatment, we used the light/dark
682 transition test and the Y-maze spontaneous alternation behavior (SAB) test. The
683 light/dark transition test is based on the innate aversion of mice to brightly illuminated
684 areas and on their spontaneous exploratory behavior in response to mild stressors
685 (Bourin & Hascoët, 2003; Takao & Miyakawa, 2006). Our results revealed that in the
686 light/dark box, HPβCD-treated mice spent less time in the brightly illuminated
687 compartment than vehicle-injected mice **(Fig. 14A)**. Additionally, HPβCD-treated mice
688 were slower to emerge from the dark compartment after being habituated to the dark for

689 30 min prior to the test **(Fig. 14A)**. These behaviors indicate decreased impulsivity and
690 behavioral disinhibition in HPβCD-treated mice.
691
692 We also assessed hippocampal-dependent spatial working memory at 7 weeks after
693 stroke with the Y-maze SAB test (Yamada et al., 1996). We discovered that vehicle-
694 injected mice developed a delayed cognitive deficit, whereas HPβCD-treated mice
695 displayed neurotypical cognitive function comparable to baseline recordings **(Fig. 14B)**.
696 To assess hippocampal edema, we measured the total hippocampal area of the
697 ipsilateral and contralateral hemispheres in aged mice that received vehicle or HPβCD.
698 Hippocampal enlargement 7 weeks after stroke was attenuated in mice that had
699 received HPβCD **(Fig. 14C)**. Through Pearson's correlation analysis, we observed a
700 moderate negative correlation (r = -0.5640) between hippocampal edema and
701 hippocampal-dependent spatial working memory outcomes in the Y-maze SAB test
702 **(Fig. 14D)**. We next evaluated secondary neurodegeneration by quantifying NeuN
703 immunoreactivity as a biomarker of secondary neurodegeneration in regions of axonal
704 degeneration. Repeated administration of HPβCD led to the preservation of NeuN
705 immunoreactivity in the striatum and thalamus **(Fig. 14E, F)**. These results demonstrate
706 that HPβCD attenuates secondary neurodegeneration and improves cognitive function
707 following stroke.
708
709 To investigate neuronal activation in hippocampal regions, we next measured the
710 immunoreactivity of c-Fos, a transcription factor thought to primarily reflect NMDA-
711 mediated neuronal activity (Albertini et al., 2018). We observed an induction of c-Fos

712 expression in the dentate gyrus, CA1, and CA3 areas of HPβCD-treated mice **(Fig.**
713 **14G)**. Importantly, Fleischmann et al. demonstrated a critical role for c-Fos in
714 hippocampal-dependent spatial learning and memory, as well as in NMDA receptor-
715 dependent LTP formation (Fleischmann et al., 2003). Together, our results show that an
716 improvement in hippocampal-dependent spatial working memory **(Fig. 14B)** is
717 associated with an induction of c-Fos in hippocampal regions of HPβCD-treated mice
718 **(Fig. 14G)** at 7 weeks after stroke.
719
720 To corroborate these findings, we further analyzed the results from the GSEA
721 performed on peri-infarct regions from vehicle- and HPβCD-treated aged mice **(Fig. 13)**.
722 We discovered that peri-infarct regions of HPβCD-treated aged mice were characterized
723 by enriched biological processes that signify improved neuronal and synaptic function,
724 including (i) long-term synaptic potentiation, (ii) neurotransmitter transport, (iii) synaptic
725 signaling, (iv) glutamate receptor activity, (v) membrane depolarization during action
726 potential, and (vi) learning or memory **(Fig. 14H)**. These results provide evidence that
727 HPβCD improves neuronal integrity in peri-infarct regions by 7 weeks after stroke.
728
729 **Discussion (1,500 words maximum, including citations)**
730
731 Dysregulated lipid homeostasis has been implicated in chronic neurodegenerative
732 diseases, including Alzheimer's disease, Parkinson's disease, and Niemann–Pick
733 disease type C, and in acute neuronal injuries, including ischemic stroke (Vance, 2012).
734 Lipid metabolism is particularly important in the mammalian brain, as lipids constitute

735 50–60% of the dry weight (Luchtman & Song, 2013). Notably, the mammalian brain is
736 highly enriched in cholesterol, which primarily exists in two distinct pools within the
737 CNS: in plasma membranes of glial cells and neurons and in myelin sheaths
738 surrounding axons. Due to the intact blood–brain barrier, cholesterol synthesis and
739 lipoprotein transport are regulated independently of the peripheral circulation (Dietschy
740 & Turley, 2001; Vance, 2012). Therefore, further investigation into the role of altered
741 lipid metabolism in neurodegeneration will likely aid in the development of novel
742 therapeutic strategies.
743
744 Our previous preclinical studies indicate that there is substantial overlap between the
745 pathological characteristics of chronic stroke infarcts and the hallmark features of
746 atherosclerotic plaques. Similar to atherosclerotic plaques, chronic stroke infarcts
747 contain foamy macrophages, lipid droplets, and intracellular and extracellular
748 cholesterol crystals (Chung et al., 2018). We have also shown that the development of
749 these pathologies coincides with the recruitment and infiltration of adaptive immune
750 cells (Doyle et al., 2015; Zbesko et al., 2021). Importantly, in atherogenesis, the
751 formation of foamy macrophages, caused by dysregulated lipid metabolic processes,
752 leads to the recruitment of adaptive immune cells and the production of cytokines and
753 degradative enzymes. Herein, we postulated that following stroke, lipids derived from
754 myelin debris and other cell membranes overwhelm the processing capability of
755 phagocytes in the brain, leading to the formation of lipid-laden foam cells, generation of
756 cholesterol crystals, secretion of pro-inflammatory cytokines, and production of
757 degradative enzymes. Further, we hypothesized that this chronic inflammatory

758 response, coupled with concurrent cell death, causes post-stroke secondary
759 neurodegeneration and impairs functional recovery.
760
761 Using the distal middle cerebral artery occlusion + hypoxia mouse model of stroke, we
762 first characterized the lipidome of chronic stroke infarcts. The lipidome of infarcts at 7
763 weeks after stroke showed a substantial elevation of lipids, including sphingomyelins,
764 sulfatides, and cholesterol esters, compared to contralateral cortices. We also observed
765 an accumulation of intracellular lipid droplets. It has been shown that the excessive
766 accumulation of cholesterol esters in lipid droplets contributes to foam cell formation (Yu
767 et al., 2013). These findings suggest that the foam cells identified in chronic stroke
768 infarcts contain an abundance of cholesterol and other myelin-derived lipids.
769
770 Using transcriptomic analyses, we assessed the impact of lipid dyshomeostasis on
771 chronic stroke infarcts and peri-infarct regions. We anticipated disparity between
772 ipsilateral and contralateral regions. Indeed, the transcriptomes of chronic stroke
773 infarcts and peri-infarct regions were characterized by an upregulation of genes
774 involved in inflammation, reactive astrogliosis, and lipid metabolism. Specifically, the
775 upregulation of TLRs, including *Tlr1*, *Tlr2*, and *Tlr4*; scavenger receptors, including
776 *Scarb2*, *Cd68*, *Msr1*, and *Cxcl16*; and other lipid mediators, including *Npc1*, *Npc2*,
777 *Lamp1*, *Ffar1*, *Pparg*, *Apoe*, *Trem2*, and *Abca1* indicates a pronounced disruption in
778 lipid homeostasis at 7 weeks after stroke. These transcriptomic analyses suggest that
779 the mechanism of foam cell formation in ischemic stroke shares commonalities with the
780 mechanism extensively characterized in atherosclerosis, albeit distinct in that myelin

781 debris, rather than circulating LDL cholesterol, appears to be the primary source of
782 lipids that overwhelm the processing capacity of infiltrating macrophages and resident
783 microglia.
784
785 We next assessed the efficacy of HPβCD in counteracting or reversing foam cell
786 formation and immune cell infiltration following stroke, as HPβCD induces liver X
787 receptor target gene expression in macrophages and leads to an increase in cholesterol
788 transporters that further promote cholesterol efflux (Zimmer et al., 2016). Cyclodextrins
789 are cyclic oligosaccharides comprised of glucose monomers. With hydrophobic interiors
790 and hydrophilic exteriors, cyclodextrins can form inclusion complexes with hydrophobic
791 compounds and yield aqueous solubility and stability across tissues. Cyclodextrins are
792 commonly utilized as carriers and solubilizing agents for steroids, antivirals, and
793 chemotherapies (Gidwani & Vyas, 2015; Rasheed et al., 2008). In addition, HPβCD has
794 also proven efficacious in the regression of atherosclerotic plaques and the prevention
795 of age-related lipofuscin accumulation (Gaspar et al., 2017; Zimmer et al., 2016). Here,
796 we found that repeated administration of HPβCD after stroke significantly attenuated
797 chronic inflammation in young adult and aged mouse models. Specifically, there were
798 substantially fewer intracellular lipid droplets, B lymphocytes, T lymphocytes, and
799 antibody-producing plasma cells in the infarcts of young adult and aged HPβCD-treated
800 mice than in vehicle-injected mice at 7 weeks after stroke.
801
802 The discovery that HPβCD is effective in attenuating B-lymphocyte accumulation in
803 chronic stroke infarcts is significant because we have shown that B lymphocytes

804 mediate cognitive dysfunction following stroke (Doyle et al., 2015). Correspondingly,
805 activated B lymphocytes and autoantibodies have been shown to cause neuropathology
806 in models of experimental autoimmune encephalomyelitis (EAE), SCI, and transient
807 middle cerebral artery occlusion (Ankeny et al., 2006; Ortega et al., 2015; Raine et al.,
808 1999). However, the B-lymphocyte response to stroke is heterogeneous and has also
809 been shown to be beneficial for stroke recovery. For example, it consists of both T-
810 lymphocyte dependent and T-lymphocyte independent responses (Weitbrecht et al.,
811 2021; Zbesko et al., 2021). Additionally, B-lymphocyte depletion following stroke
812 reduces stroke-induced hippocampal neurogenesis and impairs functional recovery
813 (Ortega et al., 2020). Future studies are necessary to elucidate the role of infiltrating B
814 lymphocytes in stroke recovery.
815
816 Using transcriptomic analyses, we next assessed transcripts in infarct and peri-infarct
817 regions of HPβCD-treated aged mice. We found that systemic administration of HPβCD
818 distinctively altered the transcriptomes of infarct and peri-infarct regions. In infarcts,
819 HPβCD upregulated genes involved in lipid metabolic processes, including *Lipa*, *Npc1*,
820 *Apoe*, and *Abca1*; in peri-infarct regions, HPβCD had an inverse effect on these genes.
821 These observations suggest that HPβCD has supported the restoration of lipid
822 homeostasis through transcriptional reprogramming of macrophages, consistent with a
823 previously described mechanism of action (Zimmer et al., 2016). In addition, HPβCD
824 influenced expression profiles in infarcts through the upregulation of genes involved in
825 angiogenesis and in peri-infarct regions through the upregulation of genes involved in

826 neuronal and synaptic structure and function. Together, these results indicate that
827 HPβCD exerts multiple restorative effects on affected brain regions after stroke.
828
829 We next evaluated the efficacy of HPβCD in enhancing recovery after stroke. We
830 assessed impulsivity and risk-taking behavior using the light/dark transition test. We
831 have previously demonstrated a chronic impact of stroke on the psychological
832 measurement of impulsivity in the light/dark transition test, resembling the uninhibited,
833 risk-taking behaviors exhibited by patients with Alzheimer and frontotemporal dementias
834 (Liscic et al., 2007; Nguyen et al., 2018). HPβCD-treated mice spent less time in the
835 brightly illuminated chamber and were slower to exit the dark chamber. These behaviors
836 suggest that HPβCD-treated mice act less erratically and impulsively than vehicle-
837 injected mice. We also measured hippocampal-dependent spatial working memory
838 using the Y-maze spontaneous alternation behavior test. We found that vehicle-injected
839 mice developed a delayed cognitive deficit, whereas HPβCD-treated mice displayed
840 neurotypical cognitive function. This improvement in recovery was associated with a
841 reduction in hippocampal edema, a preservation of neurons in the striatum and
842 thalamus, and an induction of c-Fos expression in hippocampal regions (dentate gyrus,
843 CA1, CA3). Correspondingly, peri-infarct regions of HPβCD-treated mice were defined
844 by an enrichment of biological processes signifying improved neuronal and synaptic
845 integrity. Thus, administration of HPβCD reduced stroke-induced neuropathology and
846 improved cognitive function after stroke.
847

848 For decades, putative neuroprotectants have failed in clinical stroke trials despite
849 demonstrating efficacy in preclinical studies. In light of these failures, we followed
850 Stroke Therapy Academic Industry Roundtable (STAIR) guidelines to accelerate the
851 translation of HPβCD from bench to bedside (Landis et al., 2012; Lapchak et al., 2012;
852 STAIR, 1999): (i) we performed and analyzed experiments in a randomized and blinded
853 manner; (ii) we calculated sample sizes based on a power analysis prior to the start of
854 the study; (iii) we delayed treatment by 1 week to achieve an optimal therapeutic time
855 window; (iv) we selected a dosage and a systemic route of administration to parallel
856 preclinical trials using HPβCD in Niemann–Pick disease type C; (v) we chose a model
857 of stroke in which long-term functional outcomes could be assessed; and (vi) we utilized
858 both young adult and aged animals. However, there are additional experiments that
859 need to be conducted. For example, we have not yet tested the efficacy of HPβCD in
860 female mice. Although we anticipate comparable efficacy in females, future studies are
861 needed to address sex as a biological variable. In addition, HPβCD must still be tested
862 in a model of transient occlusion, in a different laboratory, and in a second species.
863
864 In conclusion, we have shown that, coincident with the progressive infiltration of
865 adaptive immune cells, chronic stroke infarcts accumulate lipids, including
866 sphingomyelins, sulfatides, and cholesterol esters. To our knowledge, this substantial
867 disruption in lipid homeostasis has not been previously recognized or investigated in the
868 context of stroke. We also discovered that repeated administration of HPβCD following
869 stroke aids in the restoration of lipid homeostasis, attenuates lipid droplet and immune
870 cell accumulation, and improves recovery at transcriptional and functional levels.

871 Therefore, HPβCD warrants further testing to determine if it can be repurposed for the

872 treatment of ischemic stroke and other CNS injuries.

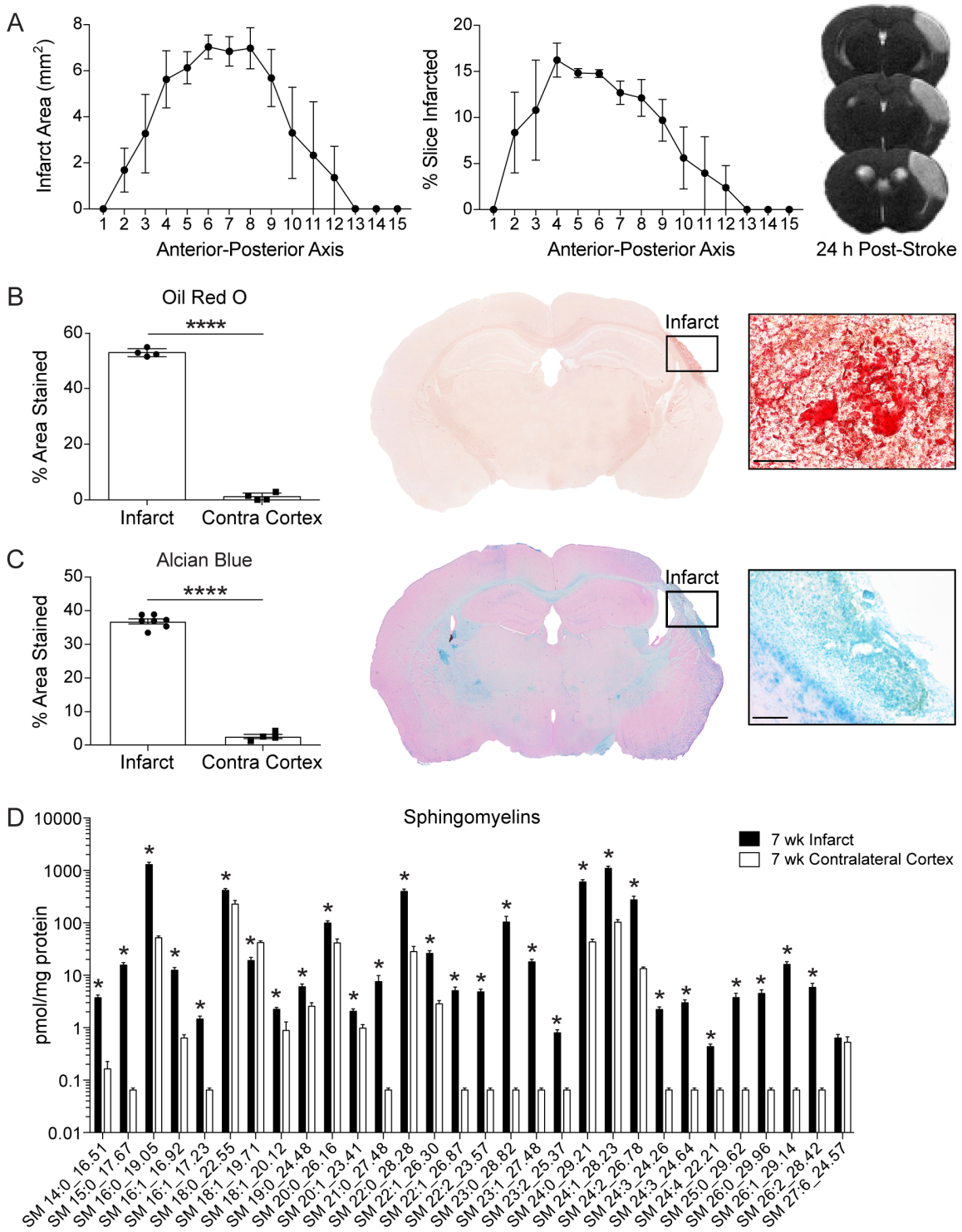

Figure 1. Lipid composition of chronic stroke infarcts in young adult mice. *A*, Infarct area per slice along the anterior-posterior axis determined by MRI at 24 h after

876 DH stroke (n = 3; 0.8 mm slice thickness). T_2-weighted images show infarcts (areas of
877 hyperintense signal) centered on the somatosensory cortex, extending to the corpus
878 callosum. ***B,*** Representative 2× and 60× images of Oil Red O staining show markedly
879 more lipid droplets in infarcts than in contralateral cortices. Scale bar, 50 μm. (n = 4;
880 paired t test; ****p < 0.0001). ***C,*** Representative 2× and 20× images of Alcian blue
881 staining show significantly more sulfatides in infarcts than in contralateral cortices. Scale
882 bar, 125 μm. ($n \geq 4$; unpaired t test; ****p < 0.0001). ***D,*** Targeted lipidomics analysis
883 revealed that infarcts had significantly higher levels of sphingomyelins than equivalent
884 regions of the contralateral cortex at 7 weeks after stroke. (n = 8; multiple t tests, Holm–
885 Sidak correction for multiple comparisons; *p < 0.05). Data are presented as mean ±
886 SEM. SM, sphingomyelin.

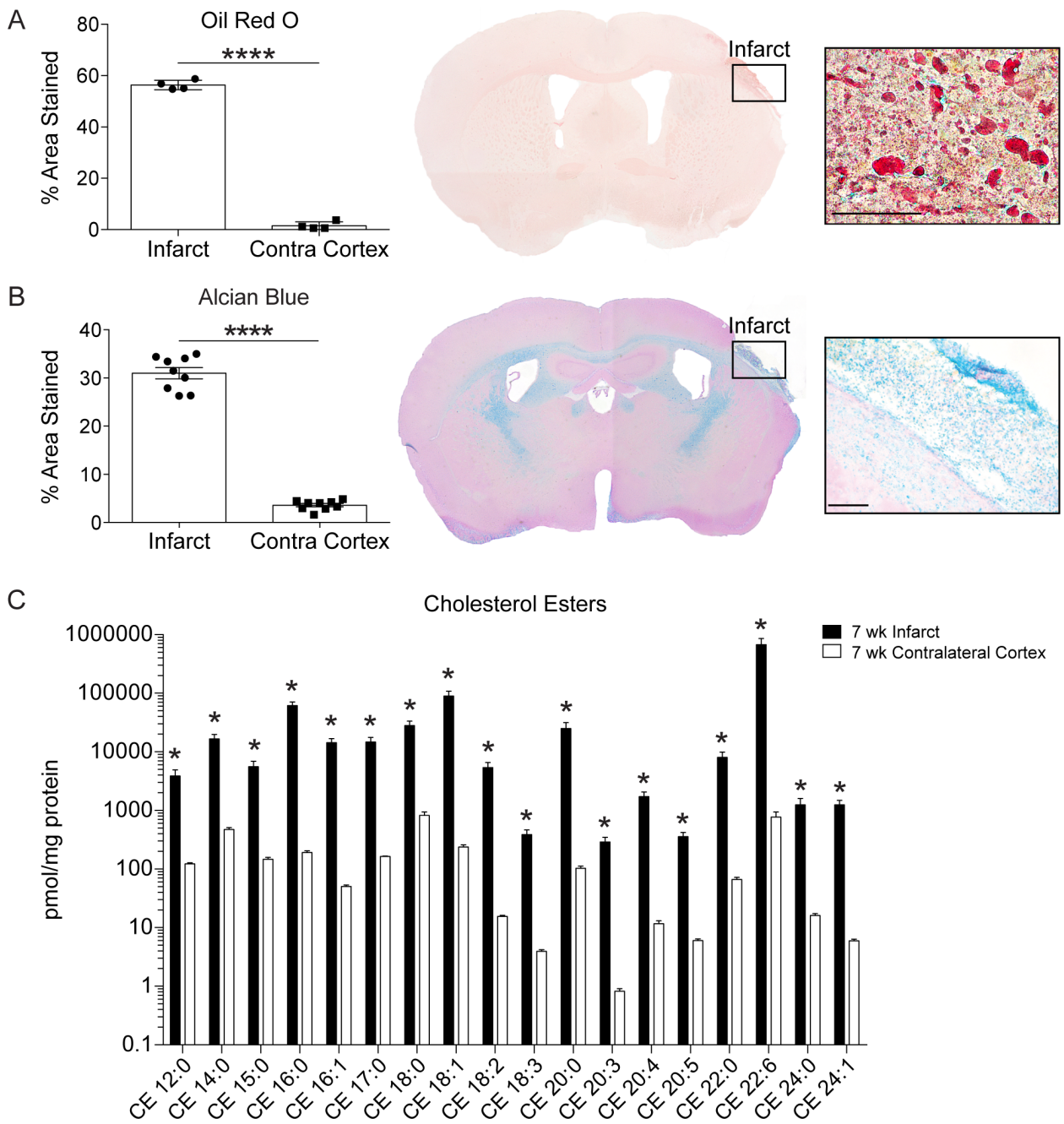

887

888 **Figure 2. Lipid composition of chronic stroke infarcts in aged mice. *A,***

889 Representative 2× and 60× images of Oil Red O staining show significantly more lipid

890 droplets in infarcts compared to contralateral cortices. Scale bar, 50 μm. (n = 4; paired t

891 tests; ****p < 0.0001). ***B,*** Representative 2× and 20× images of Alcian blue staining

892 show significantly more sulfatides in infarcts compared to contralateral cortices. Scale

893 bar, 125 μm. ($n \geq 4$; paired t tests; ****$p < 0.0001$). ***C,*** Targeted lipidomics analysis

894 revealed significantly higher levels of cholesterol esters in infarcts than in equivalent

895 regions of the contralateral cortex at 7 weeks after stroke. ($n = 5$; multiple t tests, Holm–

896 Sidak correction for multiple comparisons; *$p < 0.05$). Data are presented as mean ±

897 SEM. CE, cholesterol ester.

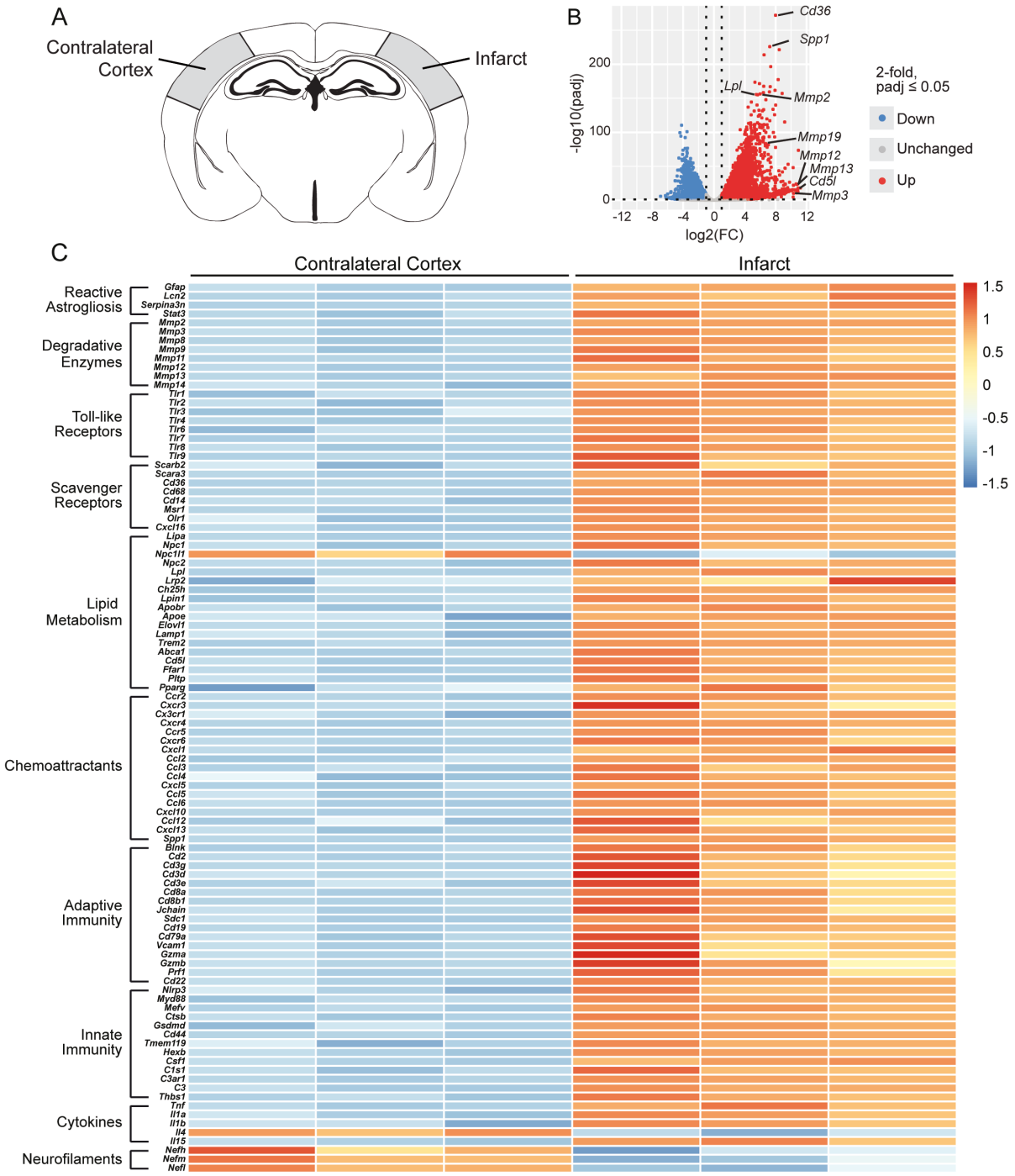

Figure 3. Transcriptome of the chronic stroke infarct in young adult mice. *A,* Schematic of a mouse coronal brain section following stroke induced by distal middle cerebral artery occlusion + hypoxia, with the analyzed region of each hemisphere

902 shaded in gray. ***B,*** Volcano plot showing differences in gene expression between the

903 infarct and contralateral cortex at 7 weeks following stroke (false discovery rate-

904 adjusted $p < 0.05$; FC > |2|). ***C,*** Row-scaled heatmap displaying differentially expressed

905 genes associated with dysregulated lipid metabolism and pronounced inflammation

906 (false discovery rate-adjusted $p < 0.05$; FC > |2|). FC, fold change.

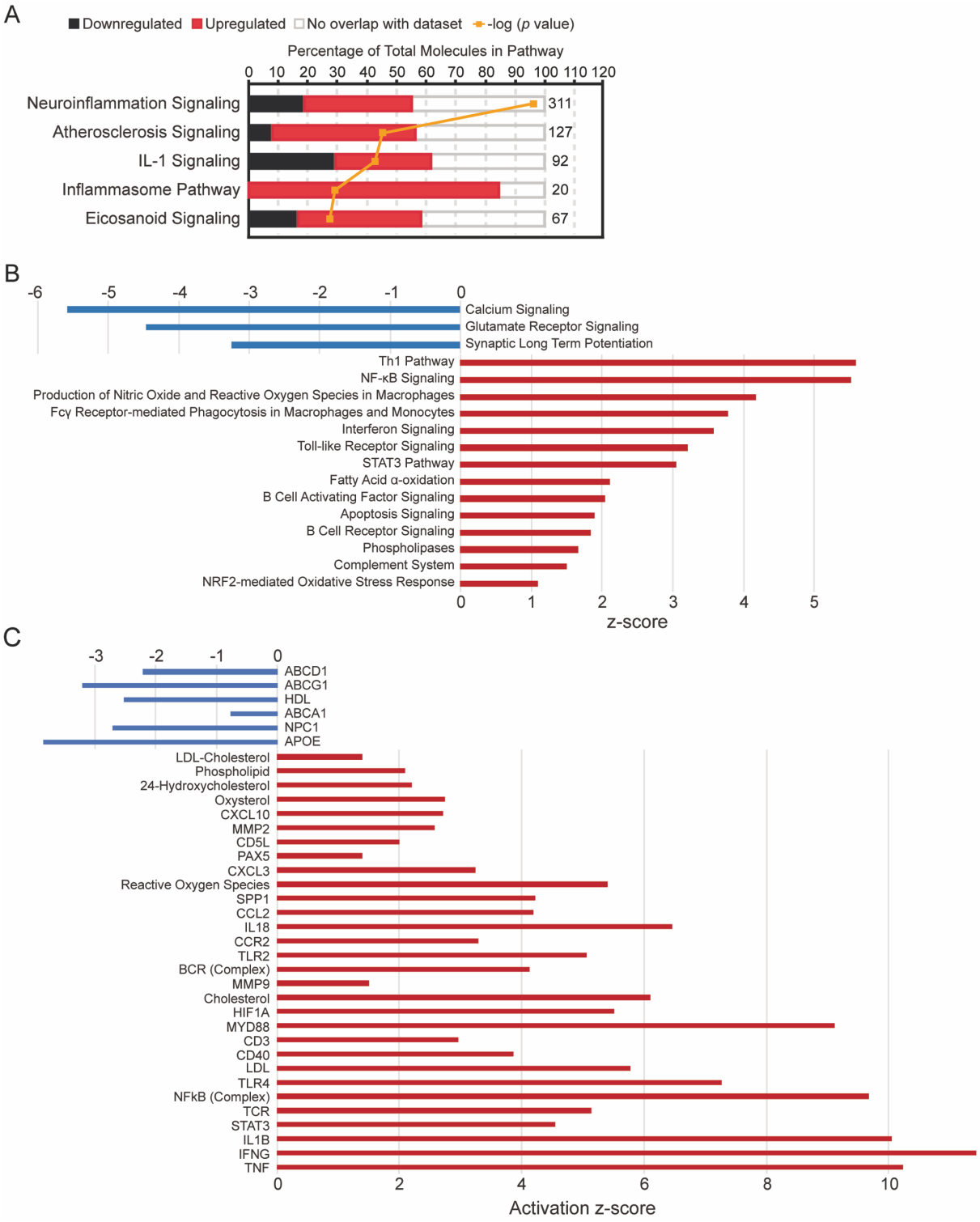

907

908 **Figure 4. Canonical pathways and upstream regulators based on differentially**

909 **expressed genes in chronic stroke infarcts of young adult mice. *A,*** Ingenuity

910 Pathway Analysis (IPA) performed on differentially expressed genes revealed a
911 significant upregulation of inflammatory pathways in infarcts of young adult mice at 7
912 weeks after stroke compared to contralateral cortices. ***B,*** Additional canonical pathway
913 analysis confirmed activation of inflammatory pathways in infarcts of young adult mice
914 at 7 weeks after stroke. ***C,*** IPA identified putative upstream regulators associated with
915 inflammation and lipid metabolism, including cholesterol, LDL, MYD88, CD3, and IL1B.
916 All canonical pathways and upstream regulators shown are significantly up- or
917 downregulated ($p < 0.05$).

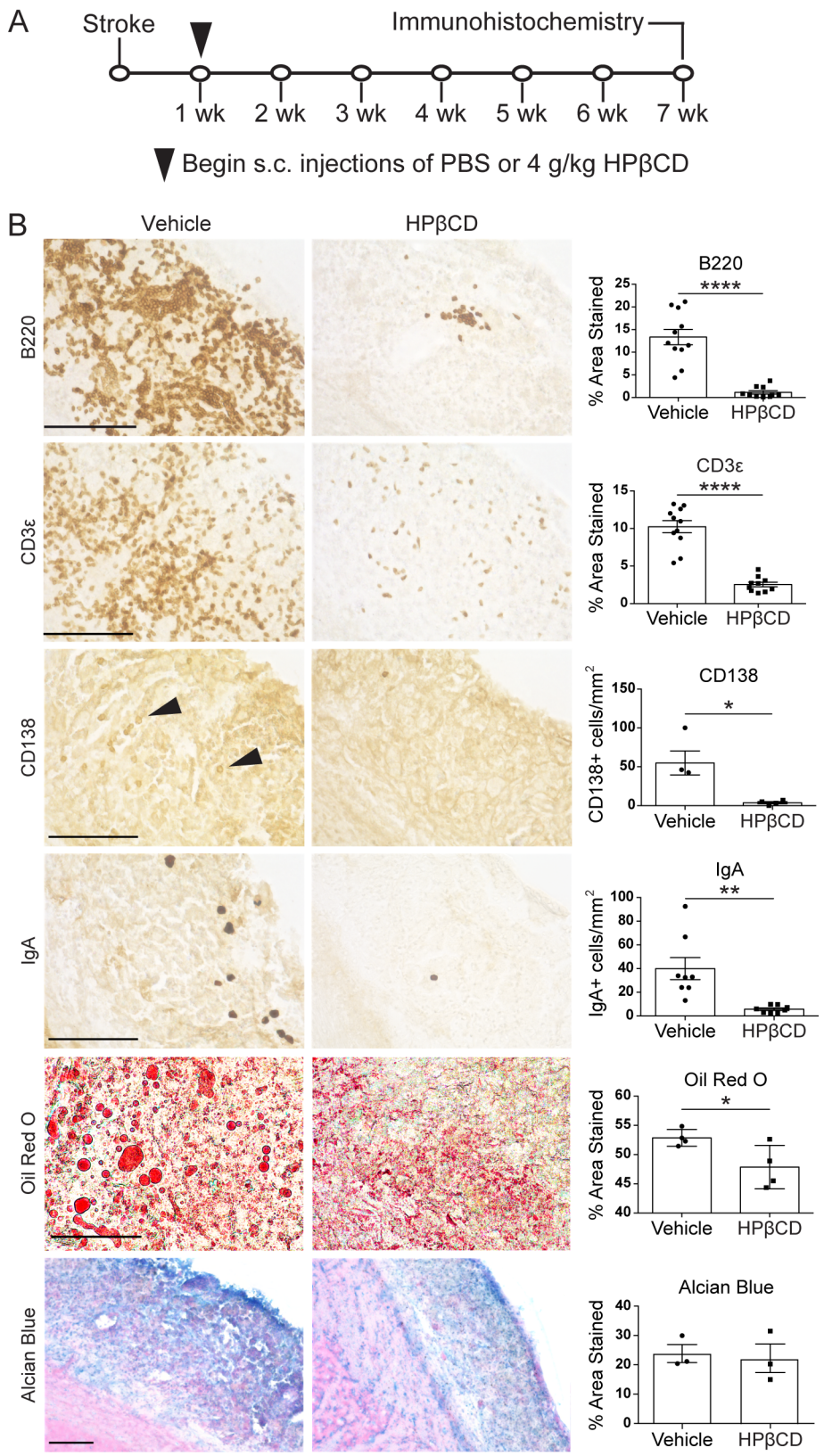
A
Stroke
Immunohistochemistry
1 wk
2 wk
3 wk
4 wk
5 wk
6 wk
7 wk
Begin s.c. injections of PBS or 4 g/kg HPβCD
B
Vehicle
HPβCD
B220
CD3ε
CD138
IgA
Oil Red O
Alcian Blue
% Area Stained
CD138+ cells/mm2
IgA+ cells/mm2
****
*
**

918

919 **Figure 5. HPβCD attenuates the chronic inflammatory response to stroke in**
920 **young adult mice**. ***A,*** Experimental design, *n* = 31–32 per group. Three-month-old
921 mice received subcutaneous (s.c.) injections of 4 g/kg HPβCD or vehicle three times a
922 week, beginning 1 week after stroke induced by distal middle cerebral artery occlusion +
923 hypoxia. Brains were extracted at 7 weeks post-stroke and processed for
924 immunohistochemistry. ***B,*** Representative 40× images of infarcts in vehicle- or HPβCD-
925 treated young adult mice stained for B lymphocytes (B220), T lymphocytes (CD3ε), and
926 antibody-producing plasma cells (CD138, IgA), followed by representative 60× images
927 of infarcts stained for lipid droplets (Oil Red O) and 20× images of infarcts stained for
928 sulfatides (Alcian blue). Quantification of images is shown to the right of each
929 photomicrograph. (*n* = 3–11; unpaired *t* tests; *$p < 0.05$, **$p < 0.01$, ****$p < 0.0001$).
930 Scale bars, 50 μm (Oil Red O), 125 μm (B220, CD3ε, CD138, IgA, Alcian blue). Data
931 are presented as mean ± SEM.

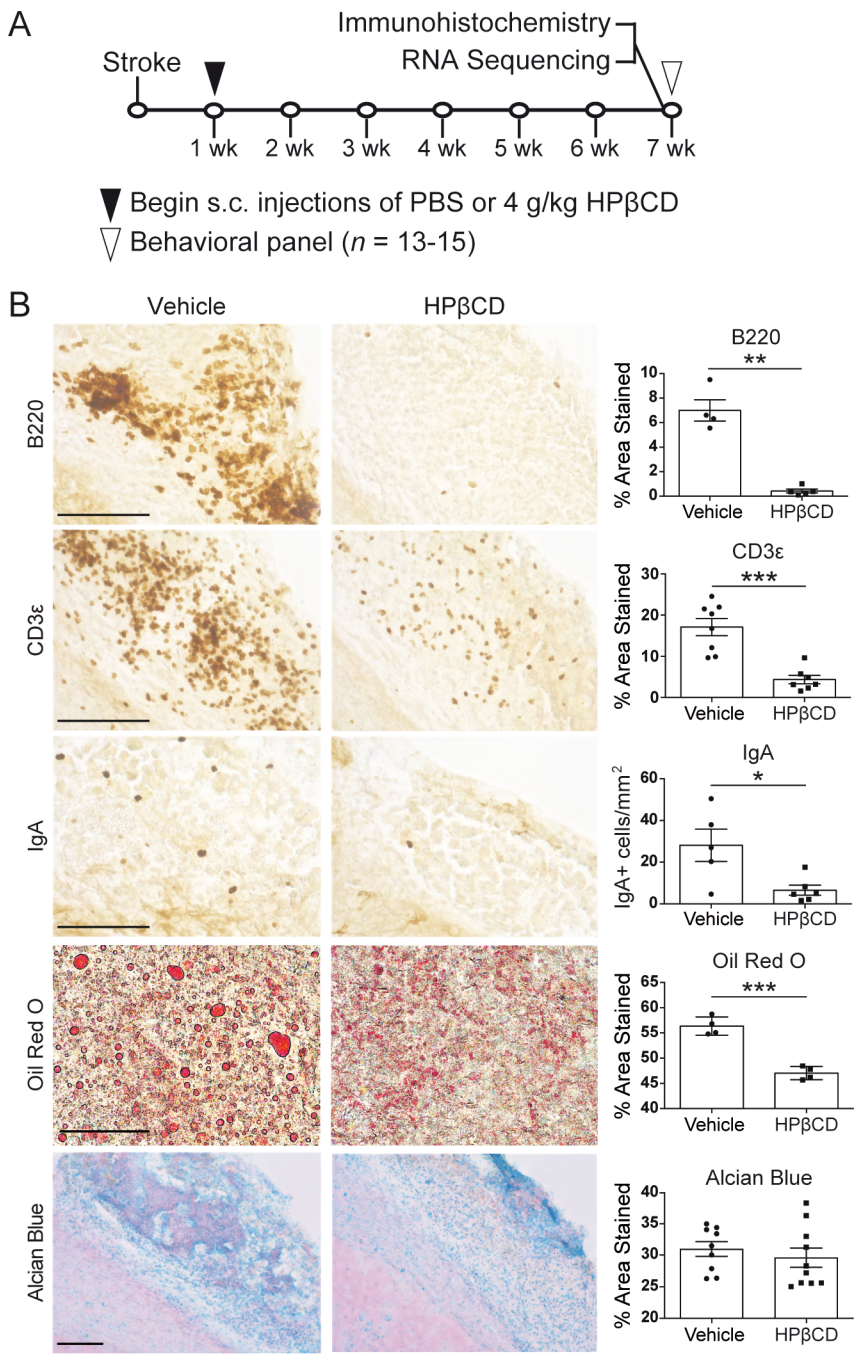

932

933 **Figure 6. HPβCD attenuates the chronic inflammatory response to stroke in aged**

934 **mice. *A,*** Experimental design, *n* = 39–40 per group. Eighteen-month-old mice received

935 subcutaneous (s.c.) injections of 4 g/kg HPβCD or vehicle three times a week,

936 beginning 1 week after stroke induced by distal middle cerebral artery occlusion +

937 hypoxia. Brains were dissected at 7 weeks post-stroke and processed for

938 immunohistochemistry or RNA-Seq. ***B,*** Representative 40× images of infarcts in

939 vehicle- or HPβCD-treated young adult mice stained for B lymphocytes (B220), T

940 lymphocytes (CD3ε), and antibody-producing plasma cells (IgA), followed by

941 representative 60× images of infarcts stained for lipid droplets (Oil Red O) and 20×

942 images of infarcts stained for sulfatides (Alcian blue).Quantification of images is shown

943 to the right of each photomicrograph. (n = 4–10; unpaired t tests; *$p < 0.05$, **$p < 0.01$,

944 ***$p < 0.001$). Scale bars, 50 μm (Oil Red O), 125 μm (B220, CD3ε, IgA, Alcian blue).

945 Data are presented as mean ± SEM.

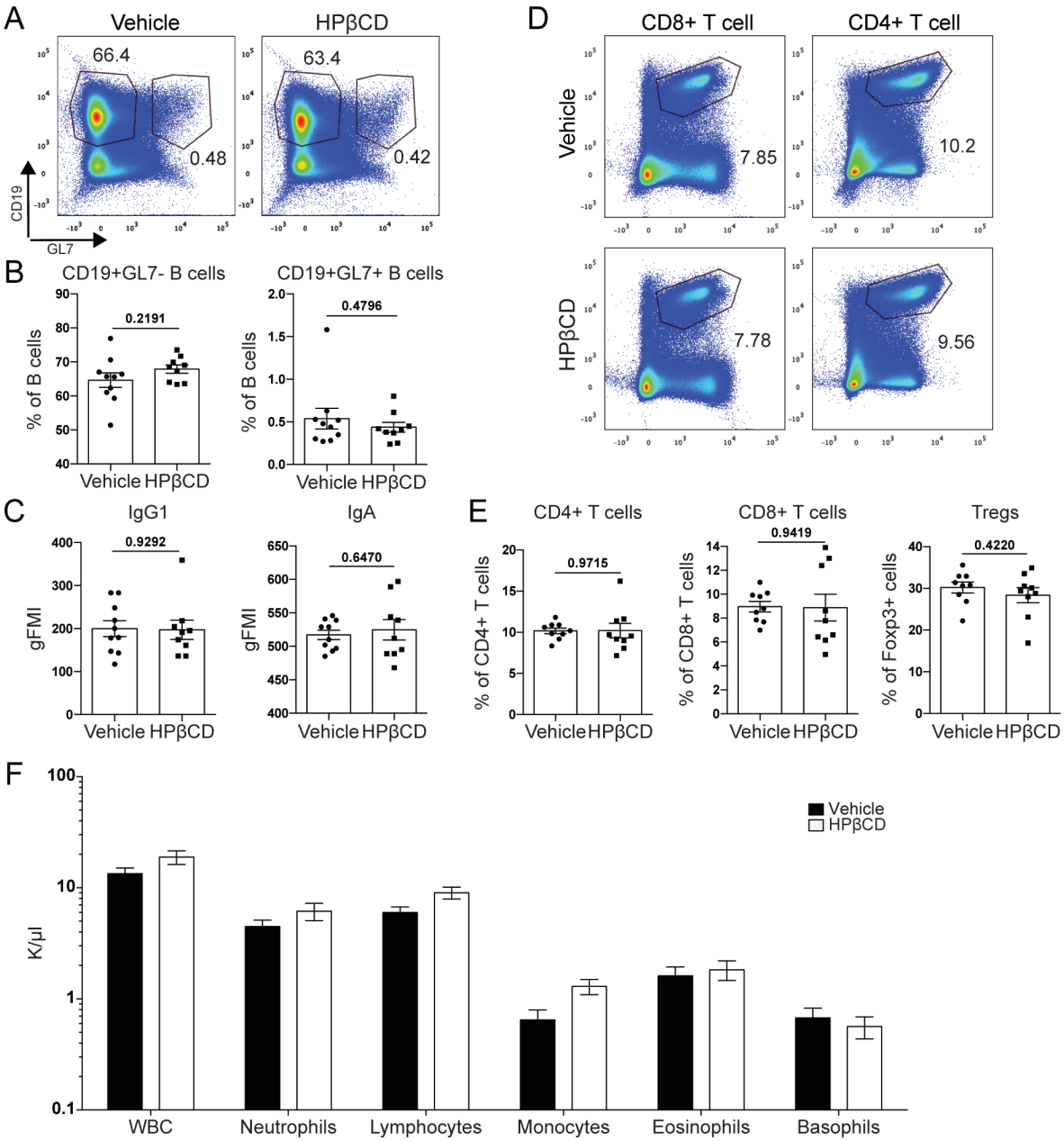

Figure 7. HPβCD does not alter peripheral immune cell populations in the blood or spleens of aged mice after stroke. *A, B,* Splenocytes from HPβCD- and vehicle-injected aged mice were stained with antibodies against CD19 and GL7. Representative flow cytometry plots (***A***) and quantification of CD19+GL7- B cells and CD19+GL7+ germinal center B cells as a percentage of total lymphocytes (***B***) showed no significant

952 differences in splenic B cell populations between vehicle- and HPβCD-treated aged
953 mice at 7 weeks after stroke. ***C,*** Quantification of antibody isotypes (IgG1 and IgA) in
954 the spleen revealed no significant differences between vehicle- and HPβCD-treated
955 aged mice at 7 weeks after stroke. ***D, E,*** Splenocytes from HPβCD- and vehicle-injected
956 aged mice were stained with antibodies against TCRβ, CD4, CD8, and Foxp3.
957 Representative flow cytometry plots of CD4+ and CD8+ T cells (***D***) and quantification of
958 CD4+ T cells, CD8+ T cells, and Tregs as a percentage of total lymphocytes (for CD4+
959 and CD8+ gates) or TCRβ+CD4+ T cells (for Treg gate) (***E***) revealed no significant
960 differences in splenic T cell populations between vehicle- and HPβCD-treated aged
961 mice at 7 weeks after stroke. (n = 9–10; unpaired t tests; *$p < 0.05$). ***F,*** Complete blood
962 count analysis in vehicle- and HPβCD-treated aged mice at 7 weeks after stroke
963 revealed no significant differences in circulating immune cell populations (n = 6; multiple
964 t tests, Holm–Sidak correction for multiple comparisons; *$p < 0.05$). Data are presented
965 as mean ± SEM. GC, germinal center.

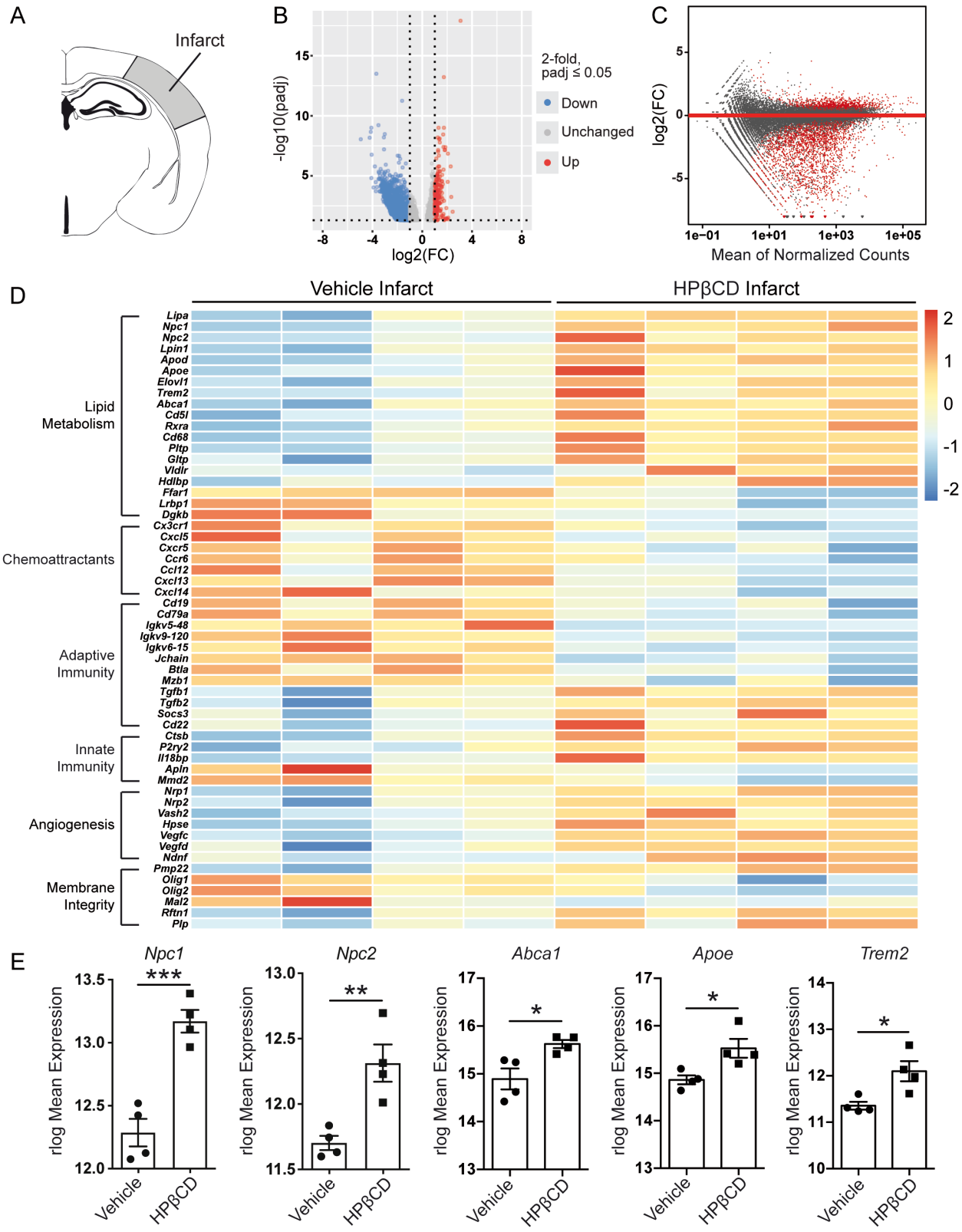
A
Infarct
B
-log10(padj)
log2(FC)
2-fold,
padj ≤ 0.05
Down
Unchanged
Up
C
log2(FC)
Mean of Normalized Counts
D
Vehicle Infarct
HPβCD Infarct
Lipid Metabolism
Chemoattractants
Adaptive Immunity
Innate Immunity
Angiogenesis
Membrane Integrity
Lipa
Npc1
Npc2
Lpin1
Apod
Apoe
Elovl1
Trem2
Abca1
Cd5l
Rxra
Cd68
Pltp
Gltp
Vldlr
Hdlbp
Ffar1
Lrbp1
Dgkb
Cx3cr1
Cxcl5
Cxcr5
Ccr6
Ccl12
Cxcl13
Cxcl14
Cd19
Cd79a
Igkv5-48
Igkv9-120
Igkv6-15
Jchain
Btla
Mzb1
Tgfb1
Tgfb2
Socs3
Cd22
Ctsb
P2ry2
Il18bp
Apln
Mmd2
Nrp1
Nrp2
Vash2
Hpse
Vegfc
Vegfd
Ndnf
Pmp22
Olig1
Olig2
Mal2
Rftn1
Plp
E
Npc1
Npc2
Abca1
Apoe
Trem2
rlog Mean Expression
Vehicle
HPβCD

966

967 **Figure 8. HPβCD promotes lipid metabolism and attenuates inflammation in**
968 **infarcts of aged mice after stroke.** ***A,*** Schematic of a mouse coronal brain section
969 following stroke induced by distal middle cerebral artery occlusion + hypoxia, with the
970 analyzed region shaded in gray. ***B, C,*** Volcano (***B***) and MA (***C)*** plots constructed from
971 count data show differences in gene expression between infarcts from vehicle- and
972 HPβCD-treated mice at 7 weeks after stroke (false discovery rate-adjusted $p < 0.05$; FC
973 > |2|). ***D,*** Row-scaled heatmap displaying differentially expressed genes associated with
974 lipid metabolism, inflammation, and angiogenesis (false discovery rate-adjusted $p <$
975 0.05; FC > |2|). ***E,*** Graphs representing rlog-normalized expression of selected genes
976 related to lipid metabolism. ($n = 4$; unpaired t tests; $^{*}p < 0.05$, $^{**}p < 0.01$, $^{***}p < 0.001$).
977 FC, fold change.

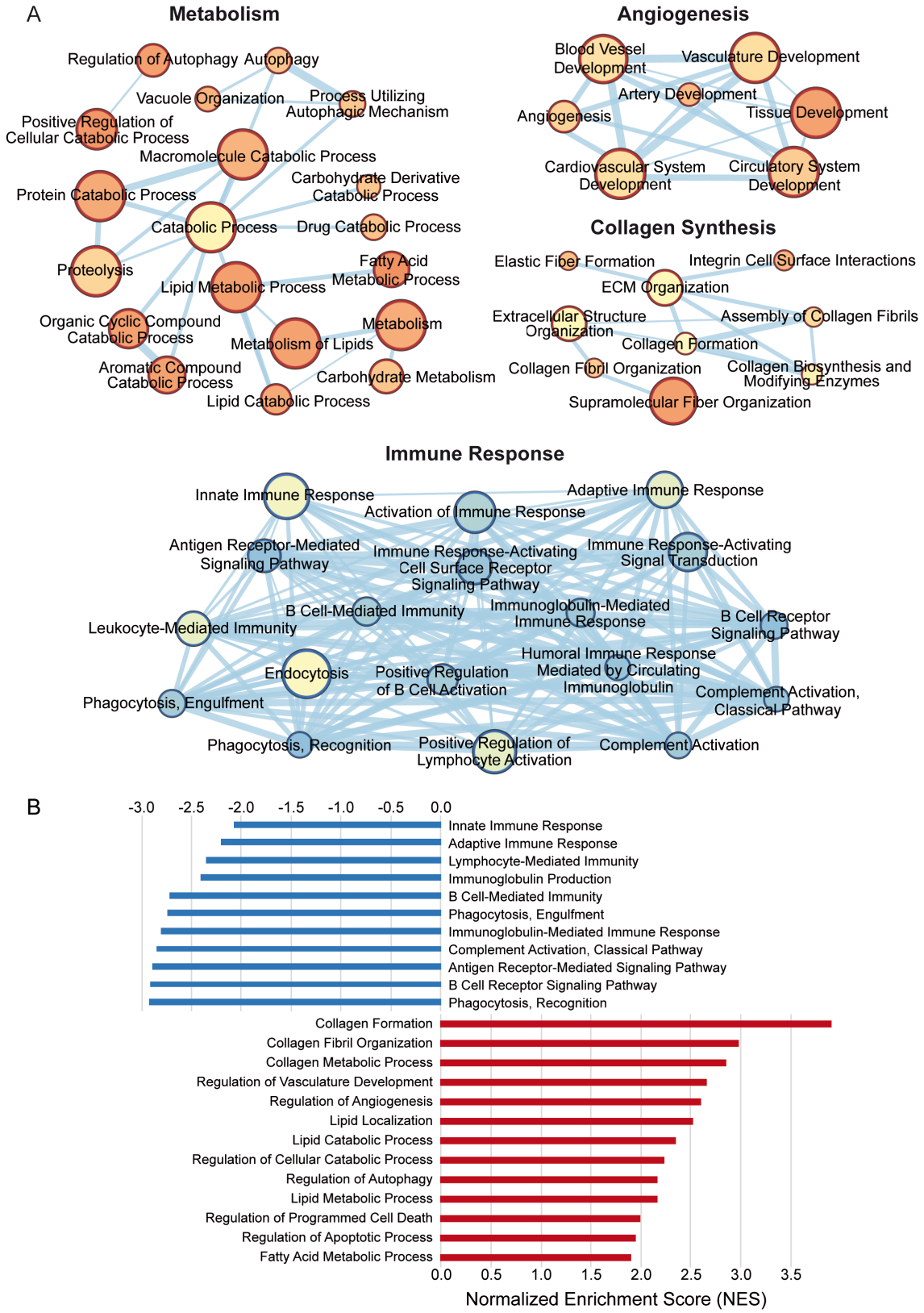
A
Metabolism
Regulation of Autophagy
Autophagy
Vacuole Organization
Process Utilizing Autophagic Mechanism
Positive Regulation of Cellular Catabolic Process
Macromolecule Catabolic Process
Carbohydrate Derivative Catabolic Process
Protein Catabolic Process
Catabolic Process
Drug Catabolic Process
Proteolysis
Fatty Acid Metabolic Process
Lipid Metabolic Process
Organic Cyclic Compound Catabolic Process
Metabolism
Metabolism of Lipids
Aromatic Compound Catabolic Process
Carbohydrate Metabolism
Lipid Catabolic Process
Angiogenesis
Blood Vessel Development
Vasculature Development
Artery Development
Angiogenesis
Tissue Development
Cardiovascular System Development
Circulatory System Development
Collagen Synthesis
Elastic Fiber Formation
Integrin Cell Surface Interactions
ECM Organization
Extracellular Structure Organization
Assembly of Collagen Fibrils
Collagen Formation
Collagen Fibril Organization
Collagen Biosynthesis and Modifying Enzymes
Supramolecular Fiber Organization
Immune Response
Innate Immune Response
Adaptive Immune Response
Activation of Immune Response
Antigen Receptor-Mediated Signaling Pathway
Immune Response-Activating Cell Surface Receptor Signaling Pathway
Immune Response-Activating Signal Transduction
B Cell-Mediated Immunity
Immunoglobulin-Mediated Immune Response
Leukocyte-Mediated Immunity
B Cell Receptor Signaling Pathway
Humoral Immune Response Mediated by Circulating Immunoglobulin
Endocytosis
Positive Regulation of B Cell Activation
Complement Activation, Classical Pathway
Phagocytosis, Engulfment
Phagocytosis, Recognition
Positive Regulation of Lymphocyte Activation
Complement Activation
B
-3.0 -2.5 -2.0 -1.5 -1.0 -0.5 0.0
Innate Immune Response
Adaptive Immune Response
Lymphocyte-Mediated Immunity
Immunoglobulin Production
B Cell-Mediated Immunity
Phagocytosis, Engulfment
Immunoglobulin-Mediated Immune Response
Complement Activation, Classical Pathway
Antigen Receptor-Mediated Signaling Pathway
B Cell Receptor Signaling Pathway
Phagocytosis, Recognition
Collagen Formation
Collagen Fibril Organization
Collagen Metabolic Process
Regulation of Vasculature Development
Regulation of Angiogenesis
Lipid Localization
Lipid Catabolic Process
Regulation of Cellular Catabolic Process
Regulation of Autophagy
Lipid Metabolic Process
Regulation of Programmed Cell Death
Regulation of Apoptotic Process
Fatty Acid Metabolic Process
0.0 0.5 1.0 1.5 2.0 2.5 3.0 3.5
Normalized Enrichment Score (NES)

978

979 **Figure 9. Biological processes enriched in infarcts of HPβCD-treated aged mice at**
980 **7 weeks after stroke.** ***A,*** Enrichment maps constructed from Gene Ontology terms
981 revealed a significant upregulation of metabolism, angiogenesis, and collagen synthesis
982 pathways and a significant downregulation of immune response pathways. Pathways
983 are shown as circles (nodes) that are connected with lines (edges) if the pathways
984 share genes. Node colors are based on the enrichment score, and edge sizes are
985 based on the number of genes shared by the connected pathways. ***B,*** Gene set
986 enrichment analysis (GSEA) revealed significant enrichment of various biological
987 processes in infarcts of HPβCD-treated aged mice, depicted in red. Conversely, GSEA
988 identified biological processes more significantly enriched in infarcts of vehicle-injected
989 mice compared to HPβCD-treated mice, depicted in blue.

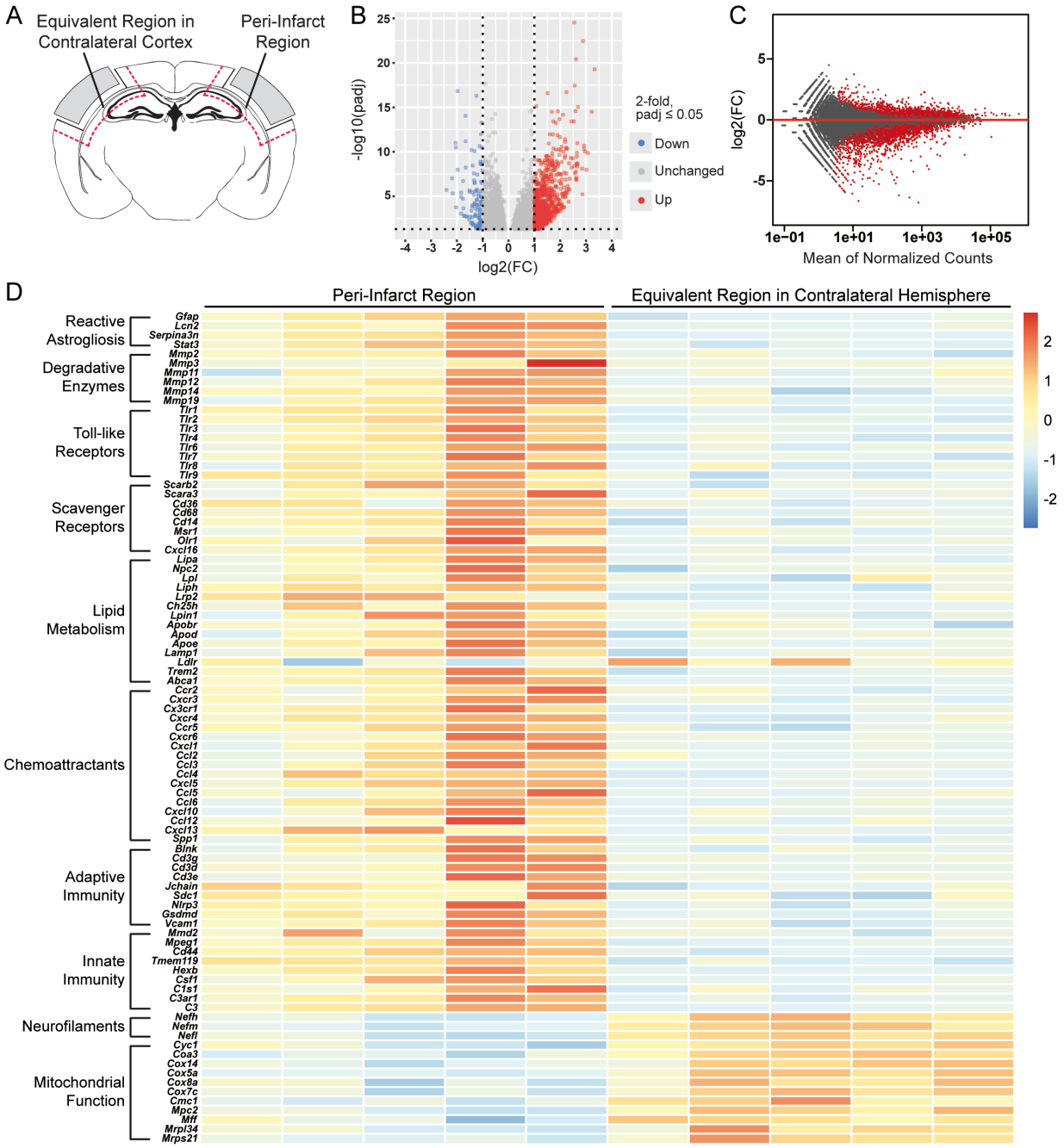

990

991 **Figure 10. Transcriptome of the peri-infarct region in aged mice at 7 weeks after**

992 **stroke. *A,*** Schematic of a mouse coronal brain section following stroke induced by

993 distal middle cerebral artery occlusion + hypoxia, with analyzed regions indicated. ***B, C,***

994 Volcano (***B***) and MA (***C***) plots constructed from count data show differences in gene

995 expression between peri-infarct regions and equivalent regions in the contralateral
996 cortex at 7 weeks after stroke (false discovery rate-adjusted $p < 0.05$; FC > |2|). ***D,*** Row-
997 scaled heatmap displaying differentially expressed genes associated with lipid
998 metabolism, inflammation, and mitochondrial function (false discovery rate-adjusted $p <$
999 0.05; FC > |2|). FC, fold change.

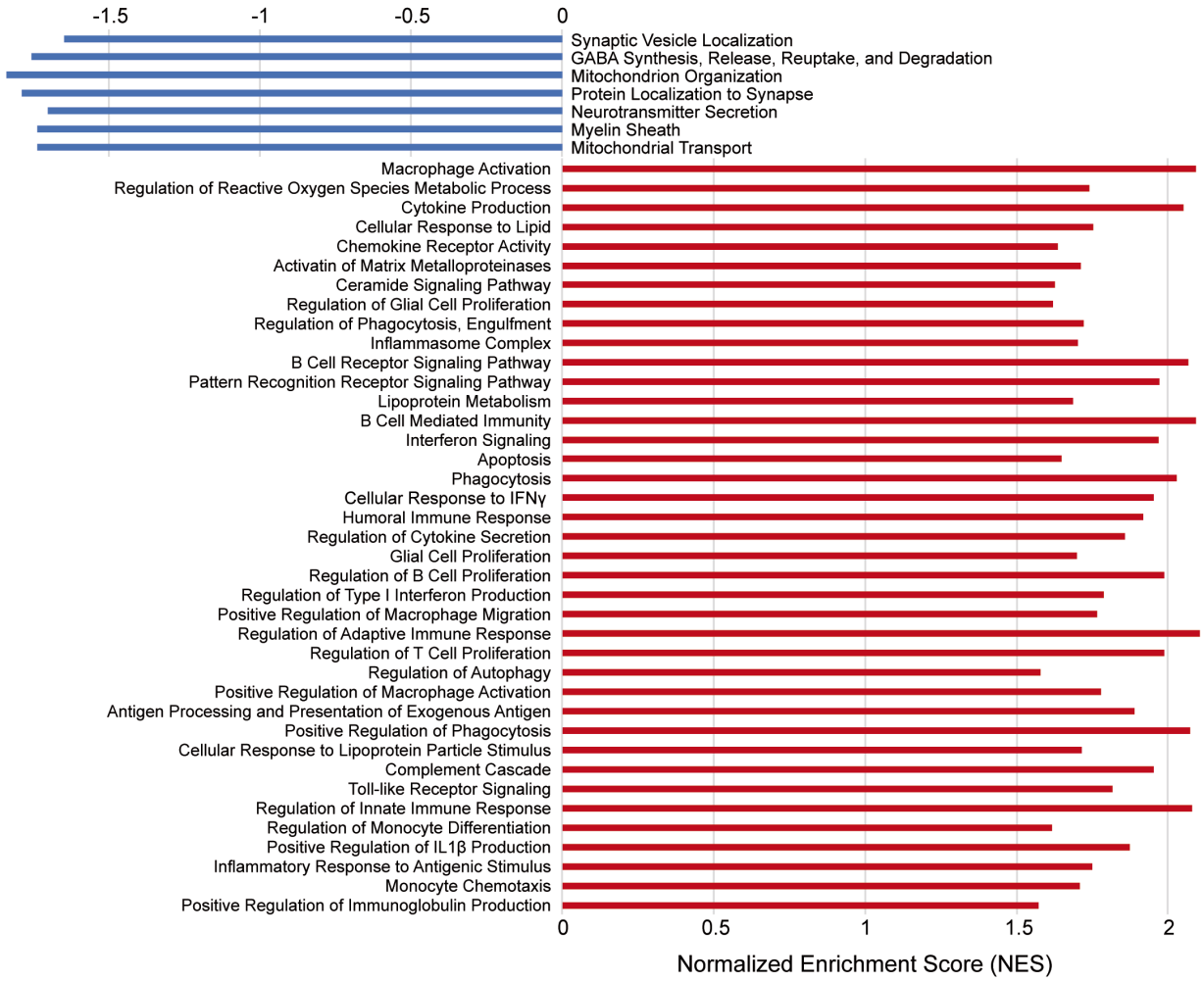

Figure 11. Biological processes enriched in peri-infarct regions of aged mice at 7 weeks after stroke. Gene set enrichment analysis (GSEA) revealed significant enrichment of multiple biological processes in peri-infarct regions of aged mice, depicted in red. Conversely, GSEA identified biological processes more significantly enriched in equivalent regions of the contralateral hemisphere, depicted in blue.

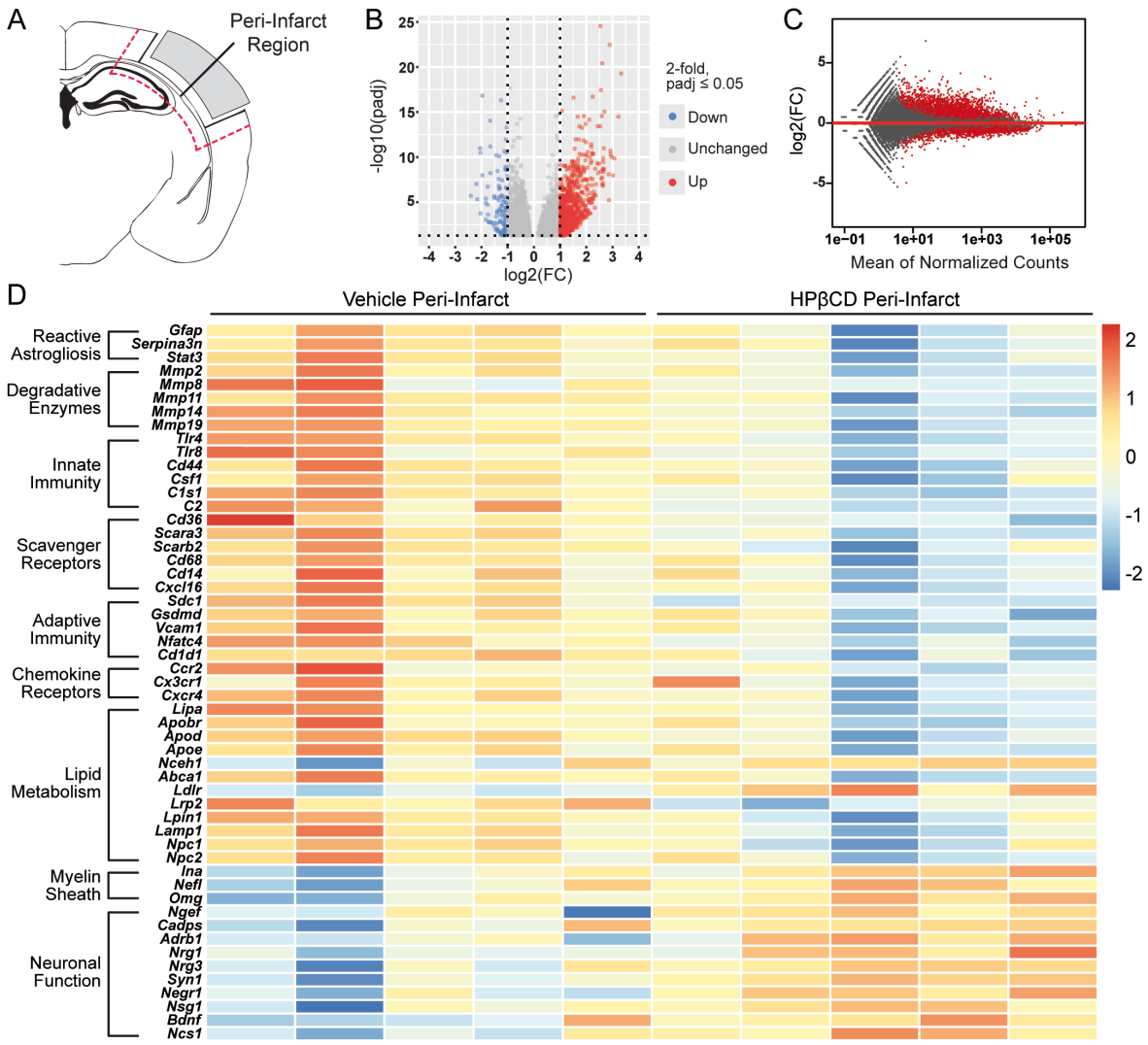

Figure 12. HPβCD attenuates inflammation and increases transcripts associated with neuronal function in peri-infarct regions of aged mice after stroke. *A,* Schematic of a mouse coronal brain section following stroke induced by distal middle cerebral artery occlusion + hypoxia, with the analyzed region indicated. ***B, C,*** Volcano (***B***) and MA (***C***) plots constructed from count data show differences in gene expression between peri-infarct regions from vehicle- and HPβCD-treated aged mice at 7 weeks after stroke (false discovery rate-adjusted $p < 0.05$; FC > |2|). ***D,*** Row-scaled heatmap

1014 displaying differentially expressed genes associated with lipid metabolism,

1015 inflammation, and neuronal function (false discovery rate-adjusted $p < 0.05$; FC > |2|).

1016 FC, fold change.

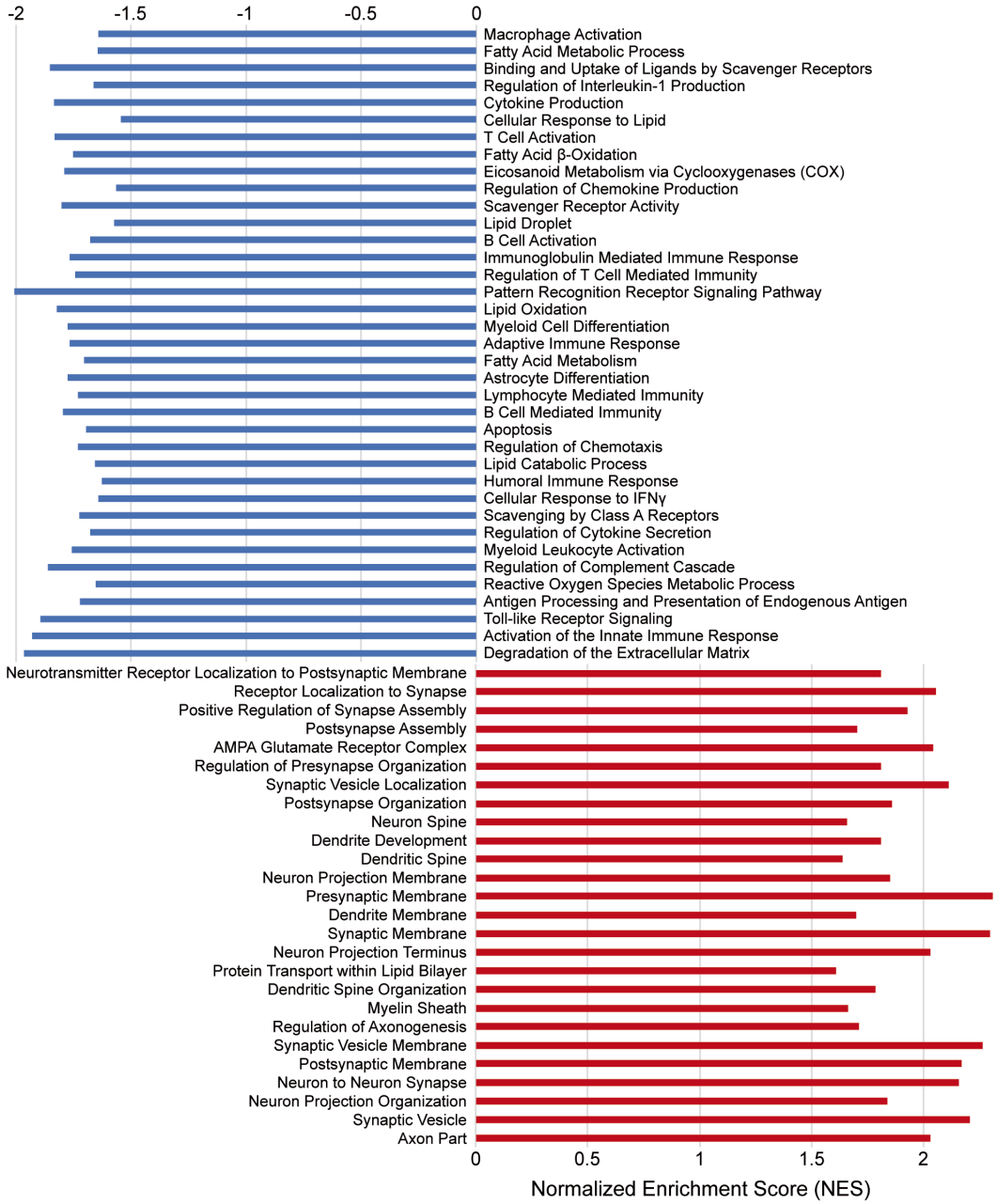

Figure 13. Biological processes enriched in peri-infarct regions of HPβCD-treated aged mice at 7 weeks after stroke. Gene set enrichment analysis (GSEA) revealed significant enrichment of multiple biological processes in peri-infarct regions of HPβCD-treated aged mice, depicted in red. Conversely, GSEA identified biological processes

1022 more significantly enriched in peri-infarct regions of vehicle-injected aged mice, depicted

1023 in blue.

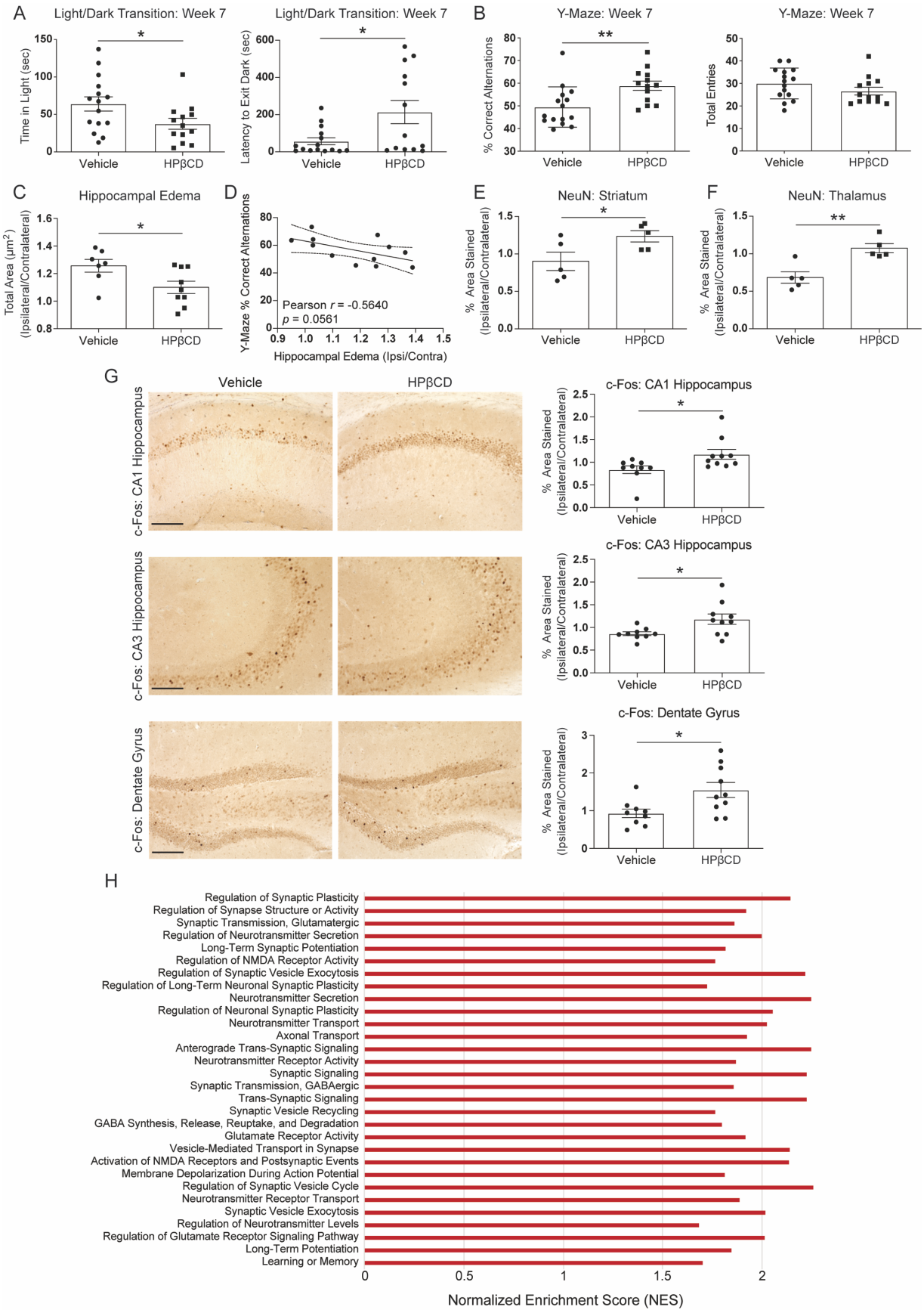
A
Light/Dark Transition: Week 7
Time in Light (sec)
Vehicle
HPβCD
Light/Dark Transition: Week 7
Latency to Exit Dark (sec)
B
Y-Maze: Week 7
% Correct Alternations
Y-Maze: Week 7
Total Entries
C
Hippocampal Edema
Total Area (μm²) (Ipsilateral/Contralateral)
D
Y-Maze % Correct Alternations
Pearson r = -0.5640
p = 0.0561
Hippocampal Edema (Ipsi/Contra)
E
NeuN: Striatum
% Area Stained (Ipsilateral/Contralateral)
F
NeuN: Thalamus
G
Vehicle
HPβCD
c-Fos: CA1 Hippocampus
c-Fos: CA3 Hippocampus
c-Fos: Dentate Gyrus
H
Regulation of Synaptic Plasticity
Regulation of Synapse Structure or Activity
Synaptic Transmission, Glutamatergic
Regulation of Neurotransmitter Secretion
Long-Term Synaptic Potentiation
Regulation of NMDA Receptor Activity
Regulation of Synaptic Vesicle Exocytosis
Regulation of Long-Term Neuronal Synaptic Plasticity
Neurotransmitter Secretion
Regulation of Neuronal Synaptic Plasticity
Neurotransmitter Transport
Axonal Transport
Anterograde Trans-Synaptic Signaling
Neurotransmitter Receptor Activity
Synaptic Signaling
Synaptic Transmission, GABAergic
Trans-Synaptic Signaling
Synaptic Vesicle Recycling
GABA Synthesis, Release, Reuptake, and Degradation
Glutamate Receptor Activity
Vesicle-Mediated Transport in Synapse
Activation of NMDA Receptors and Postsynaptic Events
Membrane Depolarization During Action Potential
Regulation of Synaptic Vesicle Cycle
Neurotransmitter Receptor Transport
Synaptic Vesicle Exocytosis
Regulation of Neurotransmitter Levels
Regulation of Glutamate Receptor Signaling Pathway
Long-Term Potentiation
Learning or Memory
Normalized Enrichment Score (NES)

1025 **Figure 14. HPβCD attenuates neurodegeneration and improves recovery in aged**
1026 **mice after stroke.** ***A,*** HPβCD-treated aged mice exhibited less impulsive behavior than
1027 vehicle-injected mice in the light/dark transition test at 7 weeks after stroke. (n = 13–15;
1028 unpaired t tests; *$p < 0.05$). ***B,*** HPβCD-treated aged mice exhibited intact spatial
1029 working memory in the Y-maze spontaneous alternation behavior test compared to
1030 vehicle-injected aged mice at 7 weeks after stroke. (n = 13–15; unpaired t tests; *$p <$
1031 0.05). ***C,*** Quantification of hippocampal edema at 7 weeks after stroke in vehicle- and
1032 HPβCD-treated mice. (n = 7–9; unpaired t test; *$p < 0.05$). ***D,*** Pearson correlation
1033 between Y-maze spontaneous alternation behavior and hippocampal edema at 7 weeks
1034 post-stroke (n = 12; r = -0.5640; $p > 0.05$). ***E, F,*** Quantification of NeuN
1035 immunoreactivity in the striatum and thalamus from vehicle- or HPβCD-treated mice. (n
1036 = 5; unpaired t tests; *$p < 0.05$, **$p < 0.01$). ***G,*** Representative 20× images of c-Fos
1037 immunoreactivity in hippocampal regions from vehicle- or HPβCD-treated mice.
1038 Quantification of images is shown to the right of each photomicrograph. (n = 9–10;
1039 unpaired t tests; *$p < 0.05$, ***$p < 0.001$). Scale bar, 125 μm. Data are presented as
1040 mean ± SEM. ***H,*** Gene set enrichment analysis revealed significant enrichment of
1041 biological processes associated with neuronal function and activity in peri-infarct regions
1042 of HPβCD-treated aged mice at 7 weeks after stroke.

Figure	Group Size (*n*)	Statistical Test	Statistical Values	*p* value	*post hoc* Comparisons	*p* value
1B	4	Paired *t* test	*M* (Contra Cortex - Infarct) = -51.71	< 0.0001	N/A	N/A
			SEM = 1.300			
1C	Infarct = 7	Unpaired *t* test	*M* (Contra Cortex - Infarct) = -34.14	< 0.0001	N/A	N/A
	Contra Cortex = 4		*SEM* = 1.077			
1D	8	Multiple *t* tests; Holm-Sidak's multiple comparisons test	N/A	N/A	SM 14:0_16.51	0.000003
					SM 15:0_17.67	< 0.000001
					SM 16:0_19.05	< 0.000001
					SM 16:1_16.92	0.000003
					SM 16:1_17.23	0.000004
					SM 18:0_22.55	0.00379
					SM 18:1_19.71	0.000172
					SM 18:1_20.12	0.009913
					SM 19:0_24.48	0.002555
					SM 20:0_26.16	0.000813
					SM 20:1_23.41	0.0018
					SM 21:0_27.48	0.006607
					SM 22:0_28.28	< 0.000001
					SM 22:1_26.30	0.000006
					SM 22:1_26.87	0.000056
					SM 22:2_23.57	0.000003
					SM 23:0_28.82	0.002919
					SM 23:1_27.48	< 0.000001
					SM 23:2_25.37	0.000017
					SM 24:0_29.21	< 0.000001
					SM 24:1_28.23	< 0.000001
					SM 24:2_26.78	0.000062
					SM 24:3_24.26	0.000002
					SM 24:3_24.64	0.000004
					SM 24:4_22.21	0.000005
					SM 25:0_29.62	0.000226
					SM 26:0_29.96	0.000076
					SM 26:1_29.14	0.000001
					SM 26:2_28.42	0.00016
2A	4	Paired *t* test	*M* (Contra Cortex - Infarct) = -54.83	< 0.0001	N/A	N/A
			SEM = 1.527			
2B	9	Paired *t* test	*M* (Contra Cortex - Infarct) = -27.39	< 0.0001	N/A	N/A

			SEM = 0.9784			
2C	5	Multiple *t* tests; Holm-Sidak's multiple comparisons test	N/A	N/A	CE 12:0	0.007817
					CE 14:0	0.000752
					CE 15:0	0.003201
					CE 16:0	0.000217
					CE 16:1	0.000495
					CE 17:0	0.001331
					CE 18:0	0.000894
					CE 18:1	0.001131
					CE 18:2	0.001921
					CE 18:3	0.001145
					CE 20:0	0.005071
					CE 20:3	0.001136
					CE 20:4	0.000936
					CE 20:5	0.000785
					CE 22:0	0.00243
					CE 22:6	0.005786
					CE 24:0	0.007793
					CE 24:1	0.000802
5B (B220)	Vehicle = 11	Unpaired *t* test	*M* (HPβCD - Vehicle) = -12.22	< 0.0001	N/A	N/A
	HPβCD = 10		*SEM* = 1.819			
5B (CD3ε)	Vehicle = 11	Unpaired *t* test	*M* (HPβCD - Vehicle) = -7.695	< 0.0001	N/A	N/A
	HPβCD = 10		*SEM* = 0.9035			
5B (CD138)	4	Unpaired *t* test	*M* (HPβCD - Vehicle) = -51.22	0.0163	N/A	N/A
			SEM = 15.49			
5B (IgA)	8	Unpaired *t* test	*M* (HPβCD - Vehicle) = -34.30	0.0026	N/A	N/A
			SEM = 9.362			
5B (ORO)	4	Unpaired *t* test	*M* (HPβCD - Vehicle) = -4.999	0.0462	N/A	N/A
			SEM = 1.995			
5B (Alcian Blue)	3	Unpaired *t* test	*M* (HPβCD - Vehicle) = -1.576	0.7977	N/A	N/A
			SEM = 5.751			
6B (B220)	Vehicle = 4	Unpaired *t* test	*M* (HPβCD - Vehicle) = -6.580	0.0039	N/A	N/A
	HPβCD = 5		*SEM* = 0.8794			
6B (CD3ε)	Vehicle = 8	Unpaired *t* test	*M* (HPβCD - Vehicle) = -12.75	0.0002	N/A	N/A
	HPβCD = 7		*SEM* = 2.429			
6B (IgA)	Vehicle = 5	Unpaired *t* test	*M* (HPβCD - Vehicle) = -21.55	0.0477	N/A	N/A

	HPβCD = 6		*SEM* = 8.139			
6B (ORO)	4	Unpaired *t* test	*M* (HPβCD - Vehicle) = -9.330 *SEM* = 1.124	0.0002	N/A	N/A
6B (Alcian Blue)	Vehicle = 9 HPβCD = 10	Unpaired *t* test	*M* (HPβCD - Vehicle) = -1.372 *SEM* = 1.954	0.4921	N/A	N/A
7B (CD19+GL 7-)	Vehicle = 10 HPβCD = 9	Unpaired *t* test	*M* (HPβCD - Vehicle) = 3.258 *SEM* = 2.553	0.2191	N/A	N/A
7B (CD19+GL 7+)	Vehicle = 10 HPβCD = 9	Unpaired *t* test	*M* (HPβCD - Vehicle) = -0.1013 *SEM* = 0.1402	0.4796	N/A	N/A
7C (IgG1)	Vehicle = 10 HPβCD = 9	Unpaired *t* test	*M* (HPβCD - Vehicle) = -2.589 *SEM* = 28.71	0.9292	N/A	N/A
7C (IgA)	Vehicle = 10 HPβCD = 9	Unpaired *t* test	*M* (HPβCD - Vehicle) = 7.567 *SEM* = 16.23	0.647	N/A	N/A
7E (CD4+ T cells)	9	Unpaired *t* test	*M* (HPβCD - Vehicle) = 0.03444 *SEM* = 0.9497	0.9715	N/A	N/A
7E (CD8+ T cells)	9	Unpaired *t* test	*M* (HPβCD - Vehicle) = -0.08889 *SEM* = 1.201	0.9419	N/A	N/A
7E (Tregs)	9	Unpaired *t* test	*M* (HPβCD - Vehicle) = -1.844 *SEM* = 2.238	0.422	N/A	N/A
7F	6	Multiple *t* tests; Holm-Sidak's multiple comparisons test	N/A	N/A	WBC Neutrophils Lymphocytes Monocytes Eosinophils Basophils	0.109564 0.213092 0.0445 0.027171 0.662546 0.58393
8E (*Npc1*)	4	Unpaired *t* test	*M* (HPβCD - Vehicle) = 0.8853 *SEM* = 0.1417	0.0008	N/A	N/A
8E (*Npc2*)	4	Unpaired *t* test	*M* (HPβCD - Vehicle) = 0.6104 *SEM* = 0.1525	0.0071	N/A	N/A
8E (*Abca1*)	4	Unpaired *t* test	*M* (HPβCD - Vehicle) = 0.7311 *SEM* = 0.2348	0.0208	N/A	N/A
8E (*Apoe*)	4	Unpaired *t* test	*M* (HPβCD - Vehicle) = 0.6647 *SEM* = 0.2186	0.0228	N/A	N/A
8E (*Trem2*)	4	Unpaired *t* test	*M* (HPβCD - Vehicle) = 0.7428	0.0187	N/A	N/A

			SEM = 0.2325			
14A (Time)	Vehicle = 15	Unpaired *t* test	*M* (HPβCD - Vehicle) = -26.63	0.0393	N/A	N/A
	HPβCD = 13		*SEM* = 12.27			
14A (Latency)	Vehicle = 15	Unpaired *t* test	*M* (HPβCD - Vehicle) = 157.5	0.0165	N/A	N/A
	HPβCD = 13		*SEM* = 61.44			
14B (% Correct Alternations)	Vehicle = 15	Unpaired *t* test	*M* (HPβCD - Vehicle) = 9.389	0.0060	N/A	N/A
	HPβCD = 13		*SEM* = 3.137			
14B (Total Entries)	Vehicle = 15	Unpaired *t* test	*M* (HPβCD - Vehicle) = -3.385	0.1847	N/A	N/A
	HPβCD = 13		*SEM* = 2.484			
14C	Vehicle = 7	Unpaired *t* test	*M* (HPβCD - Vehicle) = -0.1564	0.0311	N/A	N/A
	HPβCD = 9		*SEM* = 0.06527			
14D	12	Pearson correlation analysis	Pearson *r* = -0.5640	0.0561	N/A	N/A
			R^2 = 0.3181			
14E	5	Unpaired *t* test	*M* (HPβCD - Vehicle) = 0.3339	0.0487	N/A	N/A
			SEM = 0.1438			
14F	5	Unpaired *t* test	*M* (HPβCD - Vehicle) = 0.3901	0.0039	N/A	N/A
			SEM = 0.09717			
14G (CA1 Hippocampus)	Vehicle = 9	Unpaired *t* test	*M* (HPβCD - Vehicle) = 0.3379	0.0268	N/A	N/A
	HPβCD = 10		*SEM* = 0.1394			
14G (CA3 Hippocampus)	Vehicle = 9	Unpaired *t* test	*M* (HPβCD - Vehicle) = 0.3196	0.0229	N/A	N/A
	HPβCD = 10		*SEM* = 0.1278			
14G (Dentate Gyrus)	Vehicle = 9	Unpaired *t* test	*M* (HPβCD - Vehicle) = 0.6193	0.0178	N/A	N/A
	HPβCD = 10		*SEM* = 0.2362			

1043 **Table 1. Statistical table.**

1044 **References**

1045 Albertini, G., Walrave, L., Demuyser, T., Massie, A., De Bundel, D., & Smolders, I.
1046 (2018). 6 Hz corneal kindling in mice triggers neurobehavioral comorbidities
1047 accompanied by relevant changes in c-Fos immunoreactivity throughout the brain.
1048 *Epilepsia*, *59*(1), 67–78. https://doi.org/10.1111/epi.13943

1049 Anders, S., Pyl, P. T., & Huber, W. (2015). HTSeq-A Python framework to work with
1050 high-throughput sequencing data. *Bioinformatics*.
1051 https://doi.org/10.1093/bioinformatics/btu638

1052 Ankeny, D. P., Lucin, K. M., Sanders, V. M., McGaughy, V. M., & Popovich, P. G.
1053 (2006). Spinal cord injury triggers systemic autoimmunity: evidence for chronic B
1054 lymphocyte activation and lupus-like autoantibody synthesis. *Journal of*
1055 *Neurochemistry*, *99*(4), 1073–1087. https://doi.org/10.1111/j.1471-
1056 4159.2006.04147.x

1057 Aslanian, A. M., & Charo, I. F. (2006). Targeted disruption of the scavenger receptor
1058 and chemokine CXCL16 accelerates atherosclerosis. *Circulation*.
1059 https://doi.org/10.1161/CIRCULATIONAHA.105.540583

1060 Black, S. E. (2011). Vascular cognitive impairment: Epidemiology, subtypes, diagnosis
1061 and management. *Journal of the Royal College of Physicians of Edinburgh*, *41*(1),
1062 49–56. https://doi.org/10.4997/JRCPE.2011.121

1063 Bolger, A. M., Lohse, M., & Usadel, B. (2014). Trimmomatic: A flexible trimmer for
1064 Illumina sequence data. *Bioinformatics*.
1065 https://doi.org/10.1093/bioinformatics/btu170

1066 Bourin, M., & Hascoët, M. (2003, February 28). The mouse light/dark box test.

European Journal of Pharmacology. Elsevier. https://doi.org/10.1016/S0014-2999(03)01274-3

Cantuti-Castelvetri, L., Fitzner, D., Bosch-Queralt, M., Weil, M. T., Su, M., Sen, P., … Simons, M. (2018). Defective cholesterol clearance limits remyelination in the aged central nervous system. *Science*. https://doi.org/10.1126/science.aan4183

Chung, A. G., Frye, J. B., Zbesko, J. C., Constantopoulos, E., Hayes, M., Figueroa, A. G., … Doyle, K. P. (2018). Liquefaction of the brain following stroke shares a similar molecular and morphological profile with atherosclerosis and mediates secondary neurodegeneration in an osteopontin-dependent mechanism. *ENeuro*, *5*(5). https://doi.org/10.1523/ENEURO.0076-18.2018

Dietschy, J. M., & Turley, S. D. (2001). Cholesterol metabolism in the brain. *Current Opinion in Lipidology*. https://doi.org/10.1097/00041433-200104000-00003

Dobin, A., Davis, C. A., Schlesinger, F., Drenkow, J., Zaleski, C., Jha, S., … Gingeras, T. R. (2013). STAR: Ultrafast universal RNA-seq aligner. *Bioinformatics*. https://doi.org/10.1093/bioinformatics/bts635

Doyle, K. P., Quach, L. N., Sole, M., Axtell, R. C., Nguyen, T.-V. V., Soler-Llavina, G. J., … Buckwalter, M. S. (2015). B-Lymphocyte-Mediated Delayed Cognitive Impairment following Stroke. *Journal of Neuroscience*, *35*(5), 2133–2145. https://doi.org/10.1523/JNEUROSCI.4098-14.2015

Doyle, Kristian P., Fathali, N., Siddiqui, M. R., & Buckwalter, M. S. (2012). Distal hypoxic stroke: A new mouse model of stroke with high throughput, low variability and a quantifiable functional deficit. *Journal of Neuroscience Methods*. https://doi.org/10.1016/j.jneumeth.2012.03.003

1090 Febbraio, M., Hajjar, D. P., & Silverstein, R. L. (2001). CD36: A class B scavenger
1091 receptor involved in angiogenesis, atherosclerosis, inflammation, and lipid
1092 metabolism. *Journal of Clinical Investigation*. https://doi.org/10.1172/JCI14006
1093 Fitzner, D., Bader, J. M., Penkert, H., Bergner, C. G., Su, M., Weil, M. T., … Simons, M.
1094 (2020). Cell-Type- and Brain-Region-Resolved Mouse Brain Lipidome. *Cell*
1095 *Reports*. https://doi.org/10.1016/j.celrep.2020.108132
1096 Fleischmann, A., Hvalby, O., Jensen, V., Strekalova, T., Zacher, C., Layer, L. E., …
1097 Gass, P. (2003). Impaired long-term memory and NR2A-type NMDA receptor-
1098 dependent synaptic plasticity in mice lacking c-fos in the CNS. *Journal of*
1099 *Neuroscience*, *23*(27), 9116–9122. https://doi.org/10.1523/jneurosci.23-27-
1100 09116.2003
1101 Gaspar, J., Mathieu, J., & Alvarez, P. (2017). 2-Hydroxypropyl-beta-cyclodextrin
1102 (HPβCD) reduces age-related lipofuscin accumulation through a cholesterol-
1103 associated pathway. *Scientific Reports*. https://doi.org/10.1038/s41598-017-02387-
1104 8
1105 Ghosh, S., Zhao, B., Bie, J., & Song, J. (2010). Macrophage cholesteryl ester
1106 mobilization and atherosclerosis. *Vascular Pharmacology*.
1107 https://doi.org/10.1016/j.vph.2009.10.002
1108 Gidwani, B., & Vyas, A. (2015). A Comprehensive Review on Cyclodextrin-Based
1109 Carriers for Delivery of Chemotherapeutic Cytotoxic Anticancer Drugs. *BioMed*
1110 *Research International*. https://doi.org/10.1155/2015/198268
1111 Go, G. W., & Mani, A. (2012). Low-density lipoprotein receptor (LDLR) family
1112 orchestrates cholesterol homeostasis. *Yale Journal of Biology and Medicine*.

1113 Goldberg, I. J., Reue, K., Abumrad, N. A., Bickel, P. E., Cohen, S., Fisher, E. A., …
1114 Chen, J. (2018). Deciphering the role of lipid droplets in cardiovascular disease.
1115 *Circulation*. https://doi.org/10.1161/CIRCULATIONAHA.118.033704
1116 Landis, S. C., Amara, S. G., Asadullah, K., Austin, C. P., Blumenstein, R., Bradley, E.
1117 W., … Silberberg, S. D. (2012). A call for transparent reporting to optimize the
1118 predictive value of preclinical research. *Nature 2012 490:7419*, *490*(7419), 187–
1119 191. https://doi.org/10.1038/nature11556
1120 Lapchak, P. A., Zhang, J. H., & Noble-Haeusslein, L. J. (2012). RIGOR Guidelines:
1121 Escalating STAIR and STEPS for Effective Translational Research. *Translational*
1122 *Stroke Research 2012 4:3*, *4*(3), 279–285. https://doi.org/10.1007/S12975-012-
1123 0209-2
1124 Liscic, R. M., Storandt, M., Cairns, N. J., & Morris, J. C. (2007). Clinical and
1125 psychometric distinction of frontotemporal and Alzheimer dementias. *Archives of*
1126 *Neurology*, *64*(4), 535–540. https://doi.org/10.1001/archneur.64.4.535
1127 Love, M. I., Huber, W., & Anders, S. (2014). Moderated estimation of fold change and
1128 dispersion for RNA-seq data with DESeq2. *Genome Biology*.
1129 https://doi.org/10.1186/s13059-014-0550-8
1130 Luchtman, D. W., & Song, C. (2013). Cognitive enhancement by omega-3 fatty acids
1131 from child-hood to old age: Findings from animal and clinical studies.
1132 *Neuropharmacology*. https://doi.org/10.1016/j.neuropharm.2012.07.019
1133 Mar, F. M., da Silva, T. F., Morgado, M. M., Rodrigues, L. G., Rodrigues, D., Pereira, M.
1134 I. L., … Brites, P. (2016). Myelin Lipids Inhibit Axon Regeneration Following Spinal
1135 Cord Injury: a Novel Perspective for Therapy. *Molecular Neurobiology*.

https://doi.org/10.1007/s12035-014-9072-3

Matsuo, M., Togawa, M., Hirabaru, K., Mochinaga, S., Narita, A., Adachi, M., … Ohno, K. (2013). Effects of cyclodextrin in two patients with Niemann-Pick Type C disease. *Molecular Genetics and Metabolism*. https://doi.org/10.1016/j.ymgme.2012.11.005

Merico, D., Isserlin, R., Stueker, O., Emili, A., & Bader, G. D. (2010). Enrichment map: A network-based method for gene-set enrichment visualization and interpretation. *PLoS ONE*. https://doi.org/10.1371/journal.pone.0013984

Nguyen, T. V. V., Frye, J. B., Zbesko, J. C., Stepanovic, K., Hayes, M., Urzua, A., … Doyle, K. P. (2016). Multiplex immunoassay characterization and species comparison of inflammation in acute and non-acute ischemic infarcts in human and mouse brain tissue. *Acta Neuropathologica Communications*, *4*(1), 100. https://doi.org/10.1186/s40478-016-0371-y

Nguyen, T. V. V., Hayes, M., Zbesko, J. C., Frye, J. B., Congrove, N. R., Belichenko, N. P., … Doyle, K. P. (2018). Alzheimer's associated amyloid and tau deposition co-localizes with a homeostatic myelin repair pathway in two mouse models of post-stroke mixed dementia. *Acta Neuropathologica Communications*, *6*(1), 100. https://doi.org/10.1186/s40478-018-0603-4

Ortega, S B, Noorbhai, I., Poinsatte, K., Kong, X., Anderson, A., Monson, N. L., & Stowe, A. M. (2015). Stroke induces a rapid adaptive autoimmune response to novel neuronal antigens. *Discov Med*, *19*(106), 381–392.

Ortega, Sterling B., Torres, V. O., Latchney, S. E., Whoolery, C. W., Noorbhai, I. Z., Poinsatte, K., … Stowe, A. M. (2020). B cells migrate into remote brain areas and

support neurogenesis and functional recovery after focal stroke in mice. *Proceedings of the National Academy of Sciences*, *117*(9), 4983–4993. https://doi.org/10.1073/PNAS.1913292117

Park, Y. M. (2014). CD36, a scavenger receptor implicated in atherosclerosis. *Experimental and Molecular Medicine*. https://doi.org/10.1038/emm.2014.38

Poitelon, Y., Kopec, A. M., & Belin, S. (2020). Myelin Fat Facts: An Overview of Lipids and Fatty Acid Metabolism. *Cells*. https://doi.org/10.3390/cells9040812

Quehenberger, O., Armando, A. M., Brown, A. H., Milne, S. B., Myers, D. S., Merrill, A. H., … Dennis, E. A. (2010). Lipidomics reveals a remarkable diversity of lipids in human plasma. *Journal of Lipid Research*. https://doi.org/10.1194/jlr.M009449

Rahaman, S. O., Lennon, D. J., Febbraio, M., Podrez, E. A., Hazen, S. L., & Silverstein, R. L. L. (2006). A CD36-dependent signaling cascade is necessary for macrophage foam cell formation. *Cell Metabolism*. https://doi.org/10.1016/j.cmet.2006.06.007

Raine, C. S., Cannella, B., Hauser, S. L., & Genain, C. P. (1999). Demyelination in primate autoimmune encephalomyelitis and acute multiple sclerosis lesions: A case for antigen-specific antibody mediation. *Annals of Neurology*, *46*(2), 144–160. https://doi.org/10.1002/1531-8249(199908)46:2<144::AID-ANA3>3.0.CO;2-K

Rasheed, A., Kumar C.K., A., & Sravanthi, V. V. N. S. S. (2008). Cyclodextrins as drug carrier molecule: A review. *Scientia Pharmaceutica*. https://doi.org/10.3797/scipharm.0808-05

Schindelin, J., Arganda-Carreras, I., Frise, E., Kaynig, V., Longair, M., Pietzsch, T., … Cardona, A. (2012, July). Fiji: An open-source platform for biological-image analysis. *Nature Methods*. NIH Public Access. https://doi.org/10.1038/nmeth.2019

1182 Seifert, H. A., Hall, A. A., Chapman, C. B., Collier, L. A., Willing, A. E., & Pennypacker,
1183 K. R. (2012). A Transient Decrease in Spleen Size Following Stroke Corresponds
1184 to Splenocyte Release into Systemic Circulation. *Journal of Neuroimmune*
1185 *Pharmacology 2012 7:4*, *7*(4), 1017–1024. https://doi.org/10.1007/S11481-012-
1186 9406-8
1187 STAIR. (1999). Recommendations for standards regarding preclinical neuroprotective
1188 and restorative drug development. *Stroke*, *30*(12), 2752–2758.
1189 https://doi.org/10.1161/01.STR.30.12.2752
1190 Takao, K., & Miyakawa, T. (2006). Light/dark transition test for mice. *Journal of*
1191 *Visualized Experiments*, (1), 104. https://doi.org/10.3791/104
1192 Taylor, A. M., Liu, B., Mari, Y., Liu, B., & Repa, J. J. (2012). Cyclodextrin mediates rapid
1193 changes in lipid balance in Npc1-/- mice without carrying cholesterol through the
1194 bloodstream. *Journal of Lipid Research*. https://doi.org/10.1194/jlr.M028241
1195 Vance, J. E. (2012). Dysregulation of cholesterol balance in the brain: Contribution to
1196 neurodegenerative diseases. *DMM Disease Models and Mechanisms*.
1197 https://doi.org/10.1242/dmm.010124
1198 Virani, S. S., Alonso, A., Benjamin, E. J., Bittencourt, M. S., Callaway, C. W., Carson, A.
1199 P., … Heard, D. G. (2020). Heart disease and stroke statistics—2020 update: A
1200 report from the American Heart Association. *Circulation*.
1201 https://doi.org/10.1161/CIR.0000000000000757
1202 Weitbrecht, L., Berchtold, D., Zhang, T., Jagdmann, S., Dames, C., Winek, K., …
1203 Meisel, A. (2021). CD4+ T cells promote delayed B cell responses in the ischemic
1204 brain after experimental stroke. *Brain, Behavior, and Immunity*, *91*, 601–614.

1205 https://doi.org/10.1016/J.BBI.2020.09.029
1206 Winzeler, A. M., Mandemakers, W. J., Sun, M. Z., Stafford, M., Phillips, C. T., & Barres,
1207 B. A. (2011). The lipid sulfatide is a novel myelin-associated inhibitor of CNS axon
1208 outgrowth. *Journal of Neuroscience*. https://doi.org/10.1523/JNEUROSCI.3004-
1209 10.2011
1210 Yamada, K., Noda, Y., Hasegawa, T., Komori, Y., Nikai, T., Sugihara, H., & Nabeshima,
1211 T. (1996). The role of nitric oxide in dizocilpine-induced impairment of spontaneous
1212 alternation behavior in mice. *Journal of Pharmacology and Experimental*
1213 *Therapeutics*.
1214 Yang, Y., Hu, F., Yang, G., & Meng, Q. (2020). Lack of sphingomyelin synthase 2
1215 reduces cerebral ischemia/reperfusion injury by inhibiting microglial inflammation in
1216 mice. *Experimental and Therapeutic Medicine*, *20*(6).
1217 https://doi.org/10.3892/etm.2020.9371
1218 Yu, X. H., Fu, Y. C., Zhang, D. W., Yin, K., & Tang, C. K. (2013). Foam cells in
1219 atherosclerosis. *Clinica Chimica Acta; International Journal of Clinical Chemistry*.
1220 https://doi.org/10.1016/j.cca.2013.06.006 [doi]
1221 Zamanian, J. L., Xu, L., Foo, L. C., Nouri, N., Zhou, L., Giffard, R. G., & Barres, B. A.
1222 (2012). Genomic analysis of reactive astrogliosis. *Journal of Neuroscience*.
1223 https://doi.org/10.1523/JNEUROSCI.6221-11.2012
1224 Zbesko, J. C., Frye, J. B., Becktel, D. A., Gerardo, D. K., Stokes, J., Calderon, K., …
1225 Doyle, K. P. (2021). IgA natural antibodies are produced following T-cell
1226 independent B-cell activation following stroke. *Brain, Behavior, and Immunity*, *91*,
1227 578–586. https://doi.org/10.1016/J.BBI.2020.09.014

1228 Zbesko, J. C., Nguyen, T. V. V., Yang, T., Frye, J. B., Hussain, O., Hayes, M., … Doyle,
1229 K. P. (2018). Glial scars are permeable to the neurotoxic environment of chronic
1230 stroke infarcts. *Neurobiology of Disease*. https://doi.org/10.1016/j.nbd.2018.01.007
1231 Zeibig, S., Büttcher, M., Goebel, S., Pauli, J., Hunger, A., Ungerer, M., … Münch, G.
1232 (2019). The scavenger receptor CD68 regulates platelet mediated oxidized low-
1233 density lipoprotein (oxLDL) deposition in atherosclerotic vessels at an early stage of
1234 atherosclerosis in LDLr-/-/ApoBec-/- mice. *Cellular Physiology and Biochemistry*.
1235 https://doi.org/10.33594/000000048
1236 Zhu, Y., Lyapichev, K., Lee, D. H., Motti, D., Ferraro, N. M., Zhang, Y., … Lee, J. K.
1237 (2017). Macrophage Transcriptional Profile Identifies Lipid Catabolic Pathways That
1238 Can Be Therapeutically Targeted after Spinal Cord Injury. *The Journal of*
1239 *Neuroscience*. https://doi.org/10.1523/JNEUROSCI.2751-16.2017
1240 Zimmer, S., Grebe, A., Bakke, S. S., Bode, N., Halvorsen, B., Ulas, T., … Latz, E.
1241 (2016). Cyclodextrin promotes atherosclerosis regression via macrophage
1242 reprogramming. *Science Translational Medicine*, *8*(333).
1243 https://doi.org/10.1126/scitranslmed.aad6100
1244